ΔPSap4#5 surface-functionalized abiraterone-loaded nanoparticle successfully inhibits carcinogen-induced prostate cancer in mice: a mechanistic investigation

Ashique Al Hoque[1,2], Debasmita Dutta[2,3,4,5], Brahamacharry Paul[1], Leena Kumari[1], Iman Ehsan[1], Moumita Dhara[1], Biswajit Mukherjee[1*], Mohiuddin Quadir[2], Benny Abraham Kaipparettu[3], Soumik Laha[6] and Shantanu Ganguly[7]

*Correspondence: biswajit.
mukherjee@jadavpuruniversity.
in; biswajit55@yahoo.com

[1] Department of Pharmaceutical Technology, Jadavpur University, Kolkata 700032, India
[2] Department of Coatings and Polymeric Materials, North Dakota State University, Fargo, ND 58102, USA
[3] Department of Molecular and Human Genetics, Baylor College of Medicine, Houston, TX, USA
[4] Dana Farber Cancer Institute, Boston, MA, USA
[5] Harvard Medical School, Boston, MA, USA
[6] CSIR-Indian Institute of Chemical Biology, Kolkata 700032, India
[7] Regional Radiation Medicine Center, Thakurpukur Cancer Center, and Welfare Home Campus, Kolkata 700063, India
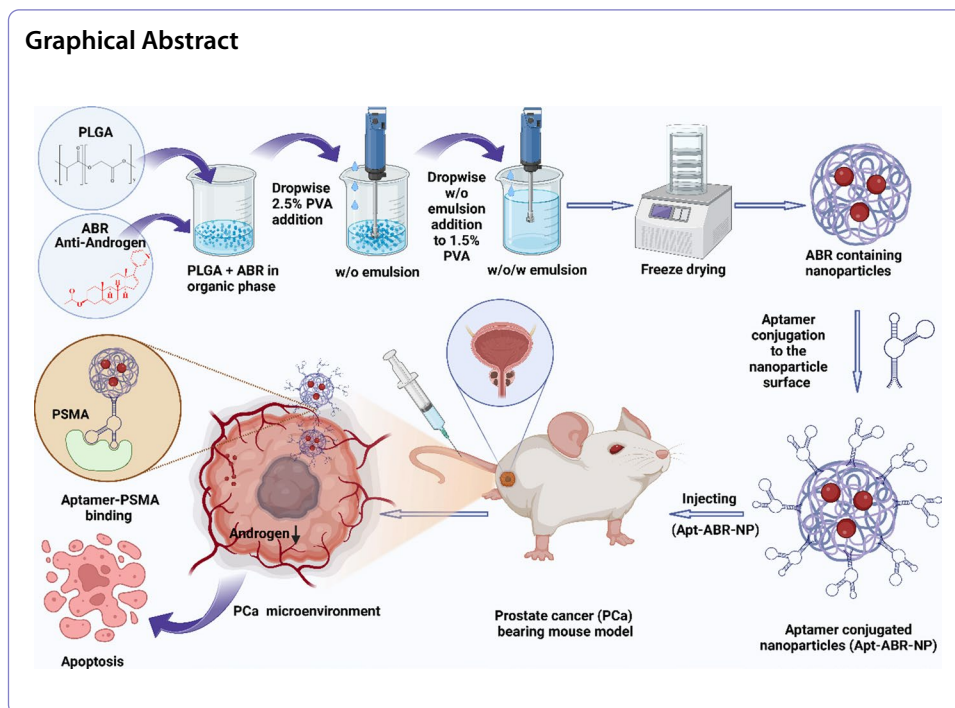
Abstract

Prostate cancer (PCa) is one of the fatal illnesses among males globally. PCa-treatment does not include radiotherapy. Chemotherapy eventually causes drug resistance, disease recurrence, metastatic advancement, multi-organ failure, and death. Pre-clinical data on PCa-induced by carcinogens are truly scarce. Although some data on xenograft-PCa in animals are available, they mostly belonged to immuno-compromised animals. Here, we developed ΔPSap4#5 aptamer surface-functionalized abiraterone-loaded biodegradable nanoparticle (Apt-ABR-NP) to investigate its targeting ability to prostate-specific membrane antigen (PSMA) in carcinogen-induced PCa mice and the therapeutic efficacy of the formulation. Aptamers are called synthetic monoclonal antibodies for their target specificity. However, they are devoid of the toxicity problem generally associated with the antibody. Abiraterone is a testosterone and androgen inhibitor, a new drug molecule that shows good therapeutic efficacy in PCa. The developed nanoparticles were physicochemically characterized and used for various in vitro and in vivo investigations. Nanoparticles had an average size of 149 nm with sustained drug release that followed Korsmeyer–Peppas kinetics. In vitro investigation showed that Apt-ABR-NP produced 87.4% apoptotic cells and 95.3% loss of mitochondrial membrane potential in LNCaP cells after 48 h of incubation. In vivo gamma scintigraphy, live imaging, and biodistribution studies in prostate cancer animal models showed the predominant targeting potential of Apt-ABR-NP. Histopathological investigation showed the remarkable therapeutic efficacy of the formulation. The pharmacokinetic study showed an increased biological half-life and enhanced blood residence time of Apt-ABR-NP. Apt-ABR-NP therapy can thus minimize off-target cytotoxicity, reduce drug loss due to site-specific delivery, and deliver abiraterone in a sustained manner to the organ of interest. Thus, the present study brings new hope for better therapeutic management of PCa in the near future.

Keywords: Aptamer-mediated tumor targeting, Prostate-specific membrane antigen (PSMA), Abiraterone acetate, Prostate cancer therapy, Pharmacokinetics

Al Hoque *et al. Cancer Nanotechnology*   (2023) 14:73

Page 2 of 34

Graphical Abstract

Introduction

Prostate cancer is the most often diagnosed cancer, having the second major cause of death from cancer after lung cancer in American men, and nearly 10 million deaths happened from the cancer only in 2020 (Sung et al. 2021). Conventional therapies such as radiation, chemotherapy, and hormone therapy cannot provide a long-term satisfactory outcome due to off-target side effects on the healthy organs and the development of drug-resistance properties after several doses of treatment regimen (Luo et al. 2019a).

Abiraterone, an active metabolite of abiraterone acetate, is a potent specific inhibitor of 17-hydroxylase/C17, 20-lyase (CYP17), a crucial enzyme in the production of testosterone and an inhibitor of androgen production in testicular, adrenal, and prostatic tumor tissues by inhibiting CYP17 (Bouhajib and Tayab 2019). The drug, BCS (Biopharmaceutics Classification System) class IV medication (Benoist et al. 2016) is a current potential treatment option for prostate cancer.

However, some inevitable limitations, such as poor solubility, permeability, and low biodistribution, make the drug difficult for its successful clinical use (Gala et al. 2020; Solymosi et al. 2018). To overcome the adverse effects and minimize the disease burden, targeted nanocarrier-mediated therapy can deliver the drug to the organ of interest to manage prostate cancer more efficiently (Fan et al. 2022).

Nanoparticle (NP) is gaining significant attraction in anticancer drug delivery (Correa et al. 2016; Ruoslahti et al. 2010). A wide range of anticancer drugs with poor pharmacokinetic properties can be delivered using nanoparticles. The site-specific delivery of drug molecules by ligand attachment to the nanoparticles can maintain drug level at an optimum therapeutic rate in a sustained manner at the target organ (Huang et al. 2021; Kabanov and Batrakova 2008; Petros and Desimone 2010; Torchilin 2007). Poly(lactic-*co*-glycolic acid) (PLGA) is one of the most widely used United States Food

and Drug Administration (FDA)-approved biodegradable polymers for systemic use. Upon its hydrolysis, it yields two monomers, lactic acid and glycolic acid (Pagels and Prud'Homme 2015). These two monomers are endogenous and rapidly metabolized by the body through the Krebs cycle; no systemic toxicity is involved in using PLGA to deliver drug or biomaterial applications (Danhier et al. 2012; Tong et al. 2012).

Targeting for antigens overexpressed on the surface of cancer cells is one of the most promising therapeutic strategies for targeting cancer cells. Among different types of targeting ligands, aptamers, the synthetic single-stranded RNA or DNA oligonucleotides (typically 25–90 nucleotide bases) with folding capacity into complex three-dimensional structures via intramolecular interactions, with target specificity, low immunogenicity, high tissue penetration ability makes them advantageous and exclusive over antibodies and other targeting molecules. Aptamers have been chosen as promising candidates for the construction of a variety of smart systems, including drug administration, treatment, diagnostics, and bioimaging (Alshaer et al. 2018; Hashemi et al. 2020; Zununi Vahed et al. 2019). Aptamers, in comparison to antibodies, have good stability in a broad pH range, temperatures, organic solvents, inexpensive, easy synthesis process, sensitivity, and great affinity to binding pockets of various target antigens (Tuerk and Gold 1990).

Preclinical data in a carcinogen-induced prostate cancer animal model are very scarce. Few such data are available in the immune-compromised prostate cancer animal xenograft model (Kato et al. 2021; Lawrence et al. 2015). However, there is no report so far available for aptamer-mediated drug targeting at the prostate-specific membrane antigen (PSMA) overexpressed in chemically induced prostate cancer in mice.

The present study was explored to investigate ΔPSap4#5 aptamer-conjugated abiraterone (ABR)-loaded PLGA nanoparticle (Apt-ABR-NP) administered by the intraperitoneal route for site-specific drug delivery to prostate cancer and to evaluate the efficacy of the formulation to inhibit prostate cancer induced by a chemical carcinogen in mice. Based on the investigated data, an effort was made to establish the formulation-mediated prostate cancer inhibitory mechanism. Aptamer–prostate cancer antigen binding ability was tested by molecular docking.

Experimental section

Materials

Poly (D, L-lactic-*co*-glycolic acid) (PLGA) (75:25), fluorescein isothiocyanate (FITC), and 3-(4, 5-dimethylthiazol-2-yl)-2, 5-diphenyltetrazolium bromide (MTT dye) were procured from Sigma-Aldrich Co., St Louis, MO, USA. Abiraterone acetate was obtained from MSN laboratories, Hyderabad, Telangana, India, as a gift sample. *N*-Hydroxysuccinimide (NHS), and 1-(3-dimethylaminopropyl)-3-ethylcarbodiimide hydrochloride (EDC) were purchased from Himedia Laboratories (Mumbai, Maharashtra, India). Prostate carcinoma cells, LNCaP, and PC3 cells were procured from National Centre for Cell Science (NCCS), Pune, India. The human prostate cancer cell line, 22Rv1 was obtained from the American Type Culture Collection (ATCC, Rockville, MD, USA). Cells were maintained in Roswell Park Memorial Institute Medium (RPMI 1640) (Hi-Media, Mumbai, Maharashtra, India). 4′,6′ Diamidino-2-phenylindole (DAPI) dye, fetal bovine serum (FBS), and other associated constituents for in vitro cell culture were obtained from Thermo Fisher Scientific, Waltham, USA. 5,5′,6,6′-Tetrachloro-1,1′,3,3′-tetraethyl
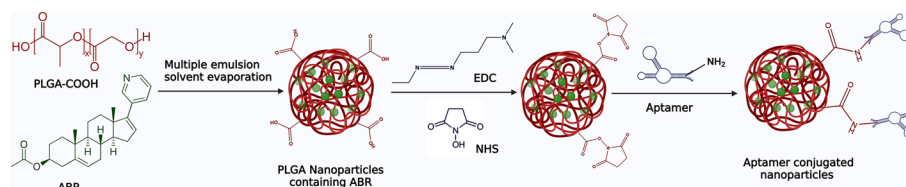
Fig. 1 Schematic representation of aptamer conjugation process to the surface of the polymeric nanoparticles containing ABR

benzimidazolylcarbocyanine iodide (JC-1) (Invitrogen, Carlsbad, CA, USA) was procured. Polyvinyl alcohol (PVA, MW 125,000) was obtained from S.D. Fine-Chem. Ltd. (Mumbai, Maharashtra, India). ΔPSap4#5 was synthesized by Eurofins Genomics India Pvt. Ltd., Bangalore, India. Testosterone propionate was purchased from Sisco Research Laboratories Pvt. Ltd. (Mumbai, India). All the chemicals were of analytical grade or molecular biology grade and used as received.

Selection of aptamer

ΔPSap4#5 (first reported by Savory et al. (2010)), A10-3.2 (first reported by Dassie et al. (2009)), A9g (first reported by Rockey et al. (2011)), and E3 (first reported by Gray et al. (2018)) are some of the widely studied aptamers used as a PSMA targeting moiety. The DNA aptamer ΔPSap4#5 (sequence: 5′-TTT TTA ATT AAA GCT CGC CAT CAA ATA GCT TT-3′) has a lower K_d value (2.6 nM) (K_d denotes the dissociation constant. The stronger is the affinity between molecules, the lower is the K_d value). Thus, ΔPSap4#5 aptamer that essentially attaches to another molecule with a low K_d strengthens the binding, and it is very much sensitive to PSMA (detection level in the picogram range) (Heydari-Bafrooei and Shamszadeh 2017; Savory et al. 2010; Souada et al. 2015; Tzouvadaki et al. 2016).

The shorter chain length also makes it easier to synthesize. The success of PSMA-ΔPSap4#5 aptamer in vitro has been reported (Heydari-Bafrooei and Shamszadeh 2017; Souada et al. 2015; Tzouvadaki et al. 2016). Hence, we have selected ΔPSap4#5 aptamer (Apt) to target PSMA with the help of ΔPSap4#5 aptamer conjugated nanosized drug delivery system.

Characterization of the ABR containing PLGA nanoparticles (ABR-NP)

Conjugation of aptamer on the surface of nanoparticles

ABR-NP was conjugated with the 3′-amino and phosphorothioate-modified aptamer through the EDC/NHS coupling method (Chakraborty et al. 2020a). Figure 1 depicts the process of conjugating aptamers onto the surface of polymeric nanoparticles containing ABR (for detailed protocol, please refer to Additional file 1).

Drug–excipient interaction study

Interaction between the drug and the chosen excipients was analyzed by using Fourier transform infrared (FTIR) spectroscopy using blank nanoparticle (nanoparticle devoid of any drug), drug (ABR), PLGA, ABR-loaded PLGA nanoparticle, and a physical mixture of drug and the excipients. In each case, the substance was mixed with I.R. grade

KBr at a 1:100 ratio and punched into pellets. They were then scanned over a range of 4000–600 cm^{-1} using an FTIR instrument (Bruker FTIR, Tensor-II, Bruker Optic GmbH, Karlsruhe, Germany).

Preparation of PLGA nanoparticles containing ABR

ABR-loaded PLGA nanoparticles and blank nanoparticles (without ABR) were prepared utilizing the multiple emulsion solvent evaporation technique according to the previously reported procedure (Chakraborty et al. 2020b). FITC-loaded and other dyes, such as Cy5 loaded nanoparticles, were made by mixing 100 μl each of a 0.4% (w/v) ethanolic dye solution into the first organic phase during the emulsion development. The detailed method of developing the nanoparticles is described in Additional file 1.

Determination of particle size and zeta potential

The average nanoparticle size and zeta potential were measured using the dynamic light scattering method. Approximately, 2 mg of ABR-NP/Apt-ABR-NP was weighed and well-dispersed in Milli-Q water (Millipore Corp., MA, USA) by sonication for 30 min in a bath sonicator (Trans-o-sonic, Mumbai, India). Finally, the particle size and zeta potential were analyzed in Malvern Zetasizer Nano-ZS 90 (Malvern Instruments, Malvern, U.K.)

Determination of surface morphology by field emission scanning electron microscopy (FESEM), atomic force microscopy (AFM), and high-resolution transmission electron microscopy (HR-TEM)

Lyophilized nanoparticles were studied with field emission scanning electron microscopy (FESEM). ABR-NP and Apt-ABR-NP were placed on a carbon stub and then coated with a thin layer of gold and scanned using FESEM. The particle morphology of hydrated nanoparticles was analyzed by AFM from 5 mg/ml of Apt-ABR-NP dispersion in Milli-Q water. The nanoparticles were then passed through 0.22-micron filters to remove any pre-existing big aggregates. Approximately 5 μl of this filtered dispersion was put on a cleaved mica sheet and air-dried for 20 min at room temperature. When the water was evaporated, a thin transparent layer formed on a mica sheet, which was seen using an AFM (5500 Agilent Technologies, Santa Clara, CA, USA) in tapping mode. The high-resolution transmission electron microscope (HR-TEM) was used to investigate internal morphology of the nanoparticles and drug distribution. On a standard carbon-coated copper grid (300 mesh), the nanoparticle suspension in Milli-Q water was dropped and allowed to air dry for 5–6 h. Image analysis was done using a high-resolution transmission electron microscope (JEOL JEM 2100 HR, Tokyo, Japan).

X-ray photoelectron spectroscopy (XPS)

The elemental composition of nanoparticles was investigated using X-ray photoelectron spectroscopy (XPS) (Luo et al. 2019b). The nanoparticle samples (ABR-NP and Apt-ABR-NP) were suspended in double distilled water, placed on a clean silicon substrate, and vacuum-dried before being examined in a Kratos Axis X-ray photoelectron spectrometer (Shimadzu, Japan) equipped with a monochromatic Al K Alpha source. The

studies employed a passage of energy of 200 eV. Spectral Data Processor v4.3 software was used to compute the elemental composition and conduct curve fitting.

Percentage of drug loading and encapsulation efficiency

Drug loading and drug encapsulation efficiencies were measured as reported earlier (Kumari et al. 2023) (for detailed method, please refer to Additional file 1):

$$\text{Theoretical drug loading (\%)} = \frac{\text{Amount of drug}}{\text{Amount of drug} + \text{excipients}} \times 100,$$

$$\text{Drug loading (actual)\%} = \frac{\text{Amount of drug in nanoparticles}}{\text{Amount of nanoparticles obtained}} \times 100,$$

$$\text{Entrapment efficiency (\%)} = \frac{\text{Drug loading (actual)(\%)}}{\text{Amount of drug loading (theoretical)(\%)}} \times 100.$$

Stability of the nanoparticles

The stability of the nanoparticles was investigated following the ICH guidelines, as reported earlier (Kumari et al. 2023) (For detailed method, refer to Additional file 1).

Hydrolytic stability study

Hydrolytic degradation of the formulation was studied in buffers of different pH (Ehsan et al. 2022). The detailed protocol has been mentioned in Additional file 1.

In vitro drug release study

In vitro drug release was conducted in phosphate buffer saline (PBS) (pH 7.4), PBS with 1% β-hydroxy cyclodextrin (pH 7.4), citrate buffer (pH 3), acetate buffer (pH 5), and bicarbonate buffer (pH 10) as per the reports published earlier (Kumari et al. 2023) (detailed method is available in Additional file 1).

Cellular studies

In vitro cellular uptake analysis by flow cytometry (FACS) and confocal microscopy

For quantitative analysis using FACS, the nanoparticles (ABR-NP and Apt-ABR-NP) were loaded with tetramethylindo(di)-carbocyanine (Cy5) to measure their comparative cellular uptake in LNCaP, 22Rv1, and PC3 cells. Briefly, LNCaP and PC3 cells were seeded in 60-mm cell culture dishes at a density of 1.5×10^6 per plate and incubated overnight in a humidified incubator at 37 °C under a 5% CO_2 environment (Wang et al. 2013). On the next day, the media were removed, Cy5 containing formulations (ABR-NP/Apt-ABR-NP) were added to the plates (except one, the 'control' group where the cells received no treatment) and incubated for different time periods (6 h and 12 h). After that, the treatment solutions were removed, and the cells were washed with PBS (pH 7.4) and redispersed in PBS (pH 7.4) in light-protected tubes. The cells were then

analyzed in a flow cytometer (BD LSR Fortessa, B.D. Biosciences) using the filter of Cy5 (excitation/emission 651 nm/670 nm).

We performed confocal laser microscopy to interpret Cy5-loaded Apt-ABR-NP uptake in LNCaP and PC3 cells (Fan et al. 2015). The study has not been performed for 22Rv1 cells. Briefly, 1.0×10^4 PC3 and LNCaP cells were seeded separately on different coverslips, and the coverslips were placed inside a 35-mm cell culture dish with adequate media (1 ml). The cells were incubated overnight at 37 ℃ and then treated with the Cy5-loaded Apt-ABR-NP for 6 h and 12 h. After treatment, the cells were washed with PBS, fixed using 70% ethanol, counter-stained with DAPI, and mounted on a slide using Prolong Diamond anti-fade-mount. The slides were then scanned under a confocal laser microscope (ZEISS LSM 900, Carl Zeiss, Oberkochen, Germany). The observation was conducted simultaneously using dual filters, Cy5 (excitation/emission 651 nm/670 nm) and DAPI (excitation/emission 359 nm/461 nm). Images were collected from individual channels and merged using ImageJ or ZEN 2012 SP2 software (ZEISS, Germany).

In vitro cell cytotoxicity assay

We studied the effect of free drug, ABR-NP and Apt-ABR-NP nanoparticles on prostate-specific membrane antigen (PSMA) overexpressing and androgen receptor (AR) positive LnCaP and 22Rv1 prostate cancer cell lines, and PC3 cells which are AR and PSMA negative. The cytotoxic effects of ABR, ABR-NP, and Apt-ABR-NP on 22Rv1, LNCaP and PC3 cells were analyzed using an MTT assay following the methods described earlier (Ehsan et al. 2022; Paul et al. 2019) (for the detailed method, see Additional file 1).

Apoptosis assay

Induction of apoptosis by ABR, ABR-NP, and Apt-ABR-NP was assessed in 22Rv1 and LNCaP cells following the Annexin V-FITC, propidium iodide (PI) dual staining method (Dutta et al. 2018; Hazra et al. 2021). Briefly, 1.5×10^6 LNCaP cells were plated in 60-mm dishes and incubated overnight in a humidified incubator with RPMI 1640 media. The media were removed on the next day, and the cells were treated with ABR, ABR-NP, and Apt-ABR-NP at their respective IC$_{50}$ concentrations in the incomplete medium (without the serum) for 48 h. Two control sets were maintained in parallel for each time point with media alone to provide the unstained and control group (PI alone). After the treatment, the media were removed, the cells were collected through trypsinization, counted to 10^5 in 100 μl binding buffer, and incubated with annexin V-FITC (5 μl) for 15 min in a dark condition. Finally, the cells were diluted to 500 μl, and 5 μl of propidium iodide was added to each tube except for the unstained group. The cells were then analyzed in a FACS instrument (BD Accuri C6, BD Bioscience, San Diego, CA) using the channels of FITC (B530-A) and propidium iodide (YG586-A). The data were plotted in a four-quadrant plot to differentiate live, early apoptotic, late apoptotic, and necrotic cells. The aptamer-conjugated nanoparticle (Apt-ABR-NP) showed the most cytotoxicity, maximum cellular uptake and maximum apoptosis induction in LNCaP cells among the experimental nanoparticles. Hence, we investigated this formulation for subsequent studies in LNCaP cells only.

Mitochondrial membrane depolarization analysis using JC-1

Mitochondrial membrane depolarization is a hallmark of apoptosis. At the initial stage of apoptosis, the mitochondrial membrane becomes depolarized (more positive), which results in a change in trans-mitochondrial membrane potential difference. This change in potential difference can be measured using a cationic dye JC-1 (5,5′,6,6′-tetrachloro-1,1′,3,3′-tetraethylbenzimidazolyl-carbocyanine iodide). In normal mitochondria (high membrane potential), JC-1 accumulates and forms J-aggregates that emit red fluorescence (~590 nm). When the mitochondrial membrane becomes depolarized (low potential), the JC-1 dye accumulates less in mitochondria, and mitochondria predominantly remain in the cytosol in a monomeric form, emitting green fluorescence (~529 nm). Hence, mitochondrial membrane depolarization can be measured using JC-1 dye by measuring an increase in green fluorescence or the green/red fluorescence intensity ratio. Standard protocol was followed for measuring fluorescence emission after JC-1 staining. Briefly, 1×10^6 LNCaP cells were seeded in 60-mm dishes, incubated overnight in a humidified incubator, and then treated with ABR, ABR-NP, and Apt-ABR-NP for 48 h. After that, the cells were removed from the dishes and incubated with 10 µl of 200 µM JC-1 in 1 ml complete media for 10 min at 37 °C in dark conditions. The media were removed by centrifugation, precipitating the cells. The cells were resuspended in PBS, pH 7.4, and were analyzed in a FACS instrument.

Clonogenic assay for the prostate cancer cell line

The in vitro cell colony formation assay was performed by determining the ability of a single cell to develop a colony after the treatment with free drug and the experimental formulations and compared with the untreated control group. LNCaP cells were seeded in 12-well plates (750 cells/well) and incubated overnight to grow (Papachristou et al. 2021). After that, the media were first replaced with the fresh complete media, and the cells were treated with ABR, ABR-NP, or Apt-ABR-NP except for the control group that received no treatment. Additionally, the media, along with the treatments, were changed in every 3 days up to the endpoint of the experiment 12–14 days, that depended on the colony numbers in control well. At the end of the treatment period, when colony confluency in control well reached the optimum level, the media or media with treatment suspensions were removed, and the cells were washed with PBS. Then 1 ml of 10% acetic acid (in methanol) was added to each plate and kept on a shaker for 10–15 min to fix the colonies. Then the cells were stained with crystal violet solution (0.5% crystal violet in 25% methanol–water) and again were shaken for 15 min under shaking conditions. Crystal violet solution was then removed, and the cells were washed with PBS three times. The plates were then air-dried overnight, and on the next day, images were captured under an optical microscope.

   After imaging, the plates were shaken with 10% acetic acid solution for 15 min to dissolve all the colonies, and with the supernatant, absorbance was measured at 510 nm using a plate reader.

In vivo animal studies

Swiss albino mice were procured from the National Institution of Nutrition (NIN), Hyderabad, India, and the complete in vivo experimental procedures with animals

Al Hoque *et al. Cancer Nanotechnology*   (2023) 14:73

Page 9 of 34

were approved by the Jadavpur University Animal Ethics Committee (JU-AEC, Protocol approval. no.: AEC/PHARM/1704/04/2020), under the norms of CPCSEA, Govt. of India (Jadavpur University Registration Number in CPCSEA: 1805/G.O./Re/S/15/CPCSEA). The guidelines of CPCSEA (Control and Supervision of Experiments on Animals) were carefully followed in all the animal experiments.

Pharmacokinetic study

In vivo pharmacokinetic studies of ABR and its nanoformulations were conducted in Swiss albino mice, having an average body weight of 25 g (Dutta et al. 2019). Mice (36 in numbers) were taken for each group. Group-I animals were treated with ABR at a dose of 400 µg/kg body weight, Group-II animals were treated with ABR-NP, and Group-III animals were treated with Apt-ABR-NP. In the cases of the formulations, a dose equivalent to the free ABR dose was administered through the formulations. Group I mice received the free drug (ABR) suspension in the water for injection through intraperitoneal injection. The formulations were directly dispersed in water for injection and injected intraperitoneally in animals of Group II and Group III, respectively. The blood samples were collected (around 1 ml from each animal) by killing three animals separately at each time point (time points taken were 2, 10, 15, 20, 30, 60, 90, 120, 240, 360, 480, 720 min) in heparin-coated tubes and were centrifuged ($10,000 \times g$ for 10 min at 4 °C) to separate the plasma (200 µl each). A volume of 500 µl of ethanol was added to each plasma sample and mixed well with a vortex mixer to dissolve the drug content. It was further centrifuged, and the clear supernatant was collected and analyzed in an LC–MS instrument (Agilent 6545 Q-TOF LC/MS system). The data were analyzed through MassLynx 4.1 software and quantified by comparing it with a calibration curve of ABR prepared. The plasma concentration *vs* time plot was generated using GraphPad Prism 5.0, and the pharmacokinetic parameters (AUC, C_{max}, T_{max}, $t_{1/2}$, MRT, V_d, CL) were calculated.

Hemolysis study

Blood samples from male Swiss albino mice were placed in heparinized tubes and centrifuged at 4 °C for 5 min at 1000g. The supernatant was removed, and the erythrocytes were washed three times in PBS (pH 7.4) before being used. The resulting suspension (2%) was employed in a hemolysis study. To test the hemolytic activity, 190 µl of the suspension was placed in each well of a 96-well plate, and a volume of 10 µl of ABR/ABR-NP/Apt-ABR-NP (with an increasing concentration of ABR, i.e., 10 to 100 µM) was added to each well. The negative control was normal saline (0% lysis), and the positive control was distilled water (100% lysis). The unlysed erythrocytes were separated by centrifugation at 10,000g for 5 min after the incubation at 37 °C for 1 h with gentle stirring. The supernatant's optical density (O.D.) was determined at 570 nm. The percent lysis was measured by comparing the O.D. value to that of the supernatant (positive control) where full lysis occurred. To acquire the average value, the tests were repeated three times (Ehsan et al. 2022; Thasneem et al. 2011).

Biodistribution study and gamma-scintigraphy imaging

In vivo biodistribution of ABR-NP and Apt-ABR-NP was studied in a Swiss albino prostate-cancer mice model using technetium-99 m (Dutta et al. 2019) radiolabeled

nanoparticles. ^{99m}Tc radiolabeling of the nanoparticles was done directly by using an acidic solution of stannous chloride (SnCl$_2$) as a reducing agent to synthesize ^{99m}Tc-labeled nanoparticles (^{99m}Tc-ABR-NP and ^{99m}Tc-Apt-ABR-NP). Mice were hydrated well with normal saline through intraperitoneal injection and anesthetized by diethyl ether. Then the radiolabelled nanoparticles containing 3.7 MBq radioactivity were injected through their tail veins. Biodistribution and gamma-scintigraphy imaging were done using ^{99m}Tc-labeled nanoparticles. The half-life of ^{99m}Tc is short (6 h) (Ramdhani et al. 2023). Hence, to get the optimum level of biodistribution and the localization of radio labeled Apt-ABR-NP, the study was conducted using intravenous route to avoid erroneous data due to the loss of radioactivity of ^{99m}Tc. In the case of pharmacokinetic and anticancer efficacy study, since no ^{99m}Tc material was involved, it was administered to animals by the intended intraperitoneal route.

For the biodistribution study, the animals were killed after 1 h, 2 h, and 5 h of post-injection through cervical dislocation. Different organs (liver, kidney, stomach, intestine, heart, lungs, and prostate) and body fluids (blood and urine) were collected in scintillation counting tubes, and radioactivities present in them were measured in a gamma-scintillation counter (ECIL, Hyderabad, India). The results were expressed as % of injected dose (% I.D.) accumulated in the organs and as % I.D. per gram (wet weight) in the case of blood. In another experiment, scintigraphy imaging was performed in live anaesthetized animals at 1 h, 2 h, and 5 h post-injection of radiolabeled nanoparticles; under a gamma-scintigraphy camera (GE Infinia) in a head-supine anterior position under static conditions. Images were analyzed using GE Infinia γ Camera facilitated along with Xeleris Work Station, Milwaukee, WI, USA (Dhara et al. 2023).

Prostate cancer development in mice, treatment undergone, and histopathological evaluation

Adult male Swiss albino mice were used to generate prostate cancer-bearing mice as described earlier (Nahata and Dixit 2012). Healthy male mice (25–30 g body weight) were procured from the National Institute of Nutrition (Hyderabad, India). They were maintained in polypropylene cages at 25 °C ± 1 °C temperature under 55% ± 5% relative humidity and normal 12 h/12 h day/night photoperiod and acclimatized with the facilities for 2 weeks before conducting any experiments. The animals were treated with subcutaneous testosterone propionate (40 mg/kg) twice a week for 12 weeks. In addition, *N*-nitroso-*N*-methyl urea (4 mg/kg) once a week was given by intraperitoneal injection as a cancer promoter for the first 4 weeks of testosterone treatment (Schleicher et al. 1996). After 12 weeks of testosterone propionate treatment, the development of prostate cancer was confirmed by histopathological observation of the prostate. A normal control group was maintained throughout the study period that received the treatment of normal saline only (the 'Normal' group, Group A).

The animals bearing prostate cancer were subdivided into four groups, one receiving normal saline only (the 'Cancer' control group, Group B), one receiving free abiraterone acetate suspension (the 'ABR' group, Group C), one receiving ABR-NP (the 'ABR-NP' group, Group D), and the last group of animals receiving Apt-ABR-NP (the 'Apt-ABR-NP' group, Group E). A minimum of 5 animals was maintained for each group. For the 'ABR', 'ABR-NP', and 'Apt-ABR-NP' groups, the dose was maintained at 100 mg/kg of ABR or equivalent through intraperitoneal injection thrice a week for 8 weeks. An additional

group of normal mice received the same treatment of Apt-ABR-NP as in the carcinogen-treated Apt-ABR-NP group of animals (Group F) to assess the impact of the formulation in normal animals. The 'Normal' and the 'Cancer control' group were treated with saline only throughout the treatment period (8 weeks). At the end of 8 weeks of treatment with ABR, ABR-NP, or Apt-ABR-NP, all the animals were killed; their prostates were isolated, fixed with formalin (4%), embedded in paraffin blocks, sectioned in thin slices (5 μm thickness), and stained with hematoxylin and eosin (H&E) for microscopic observation (Chen et al. 2020). Ki67-immunostaining was also performed in a similar way for all the 'Normal control', 'Cancer control', 'ABR-NP', and 'Apt-ABR-NP' groups. Compared to the 'Normal' group, histopathological changes in the prostates of 'Cancer', 'ABR', 'ABR-NP', and 'Apt-ABR-NP' groups were observed under an optical microscope at 10× and 40× magnifications. H&E stained sections were observed for estimation of Gleason score, lymphovascular invasion, and perineural invasion (Tătaru et al. 2021). The Gleason grading system was used to determine different patterns of tumor tissues, and scoring was carried out to represent their stages (Pierorazio et al. 2013). Ki67-stained sections were analyzed for the measurement of Ki67-positive cells using ImageJ software (version 1.53k). Areas with 3% or fewer Ki67+ cells were considered negative, with 3–25% Ki67+ cells considered as grade 1 (1+ or low grade), 26–50% Ki67+ cells were considered as grade 2 (2+ or intermediate grade), with 51–75% Ki67+ cells were considered as grade 3 (3+ high grade), and areas with 76–100% Ki67+ cells were considered as grade 4 (4+ or very high/worse grade) (Madani et al. 2011). A minimum of 10–12 images were captured for each slide for statistical analysis.

Efficacy of Apt-ABR-NP on LNCaP tumor spheroids

Single cell suspension of LNCaP cells was seeded in ultra-Low attachment plates in serum free media (DMEM/F12) with additional supplements such as 20% methyl-cellulose (Sigma), B27 (1:50, Invitrogen), 10 ng/ml bFGF (Invitrogen), 4 μg/ml insulin (Sigma), and 20 ng/ml epidermal growth factor (EGF) (Peprotech). The spheroids were generated by 7 days of cell seeding. After formation of the spheroids, one group was Cy5-loaded blank (without drug) nanoparticle control group and the other group was treated with Cy5-loaded Apt-ABR-NP for 3 consecutive days at its IC_{50} value. For the application of each dose, the media were changed with the fresh media. After completion of the treatment period, the spheroids were washed with ice cold PBS (pH 7.4) and co-stained with DAPI. Finally, photographs were taken using confocal laser microscope (Sen et al. 2023; Wolff et al. 2022).

Hematological evaluation

For complete blood count (CBC) profile of mice of the above-mentioned experimental groups of animals ("Prostate cancer development in mice, treatment undergone, and histopathological evaluation" section) were assessed. Blood from the mice were collected through cardiac puncture and whole blood was collected through cardiocentesis. Total count of red blood corpuscles (RBC), hemoglobin, hematocrit, total count of white blood cells (WBC), lymphocytes, monocytes, neutrophils, eosinophils, platelets and PSMA were analyzed using standard method (Weatherby and Ferguson 2004).

C-reactive protein (CRP) was evaluated using commercially available bioassay kits (Weldon Biotech India Pvt. Ltd., New Delhi, India).

Estimation of serum-specific toxicity markers

To determine the presence of systemic toxicity in nanoparticle-treated mice, serum biomarkers for hepatic and renal toxicity were evaluated. Each killed animal's blood was taken, and serum was extracted by centrifugation. As a hepatic toxicity marker, the serum levels of AST (aspartate aminotransferase), ALT (alanine transaminase), and alkaline phosphatase (ALP) were evaluated using commercially available bioassay kits (Coral Clinical Systems, Goa, India) following manufacturer protocols, and for nephrotoxicity, creatinine and blood urea nitrogen (BUN) were estimated using AutoZyme Creatinine kit (Accurex, Mumbai, India), and AutoZyme BUN kit (Accurex, Mumbai, India), respectively, in a UV–visible spectrophotometer (Intech-295, Advanced Microprocessor UV–Vis Single Beam) as per the manufacturer instructions.

Analysis of aptamer–PSMA interactions by molecular docking

To perform the molecular docking study, we have chosen the receptor as the PSMA to which the aptamer can bind specifically in silico. The crystal structure of PSMA, 1Z8L was obtained from the RCSB protein data bank, and the DNA aptamer structure was prepared by adding the 32-bp DNA sequence in the Discovery studio visualizer 2021 and converted to PDB format. At first, the receptor was prepared by eliminating water molecules and adding polar hydrogen atoms and charges. Then ligand molecule was also prepared for docking analysis using Discovery studio visualizer 2021. Using the HDOCK blind docking server (http://hdock.phys.hust.edu.cn/), further interactions between the aptamer and PSMA were examined (Yan et al. 2020). Providing input for the receptor and ligand was the first stage in the docking technique. The quality of a predicted protein–nucleotide binding mode was measured by its docking score. The discovery studio 2021 client program was used to conduct the docking analysis. The interactions were visualized through Biovia Discovery studio 2021 (BIOVIA Discovery Studio—BIOVIA—Dassault Systèmes®).

Statistical analysis

All the experiments were performed at least three different times, and the corresponding data were represented as the mean value along with the standard deviation. Statistical analysis of data was performed using Student's *t*-test, Dunnett's test, and one-way ANOVA, followed by Tukey's post hoc test, two-way ANOVA analysis, and tested by Bonferroni's post-test. The images, graphical, and bar diagrammatic representations were accomplished using various software such as Origin 2021, Graph Pad Prism software (version 5, Graph Pad Prism software Inc, San Diego, CA, USA), Gimp 2.10.30, ImageJ, AutoDock 4.2, and BIOVIA Discovery Studio Visualizer. Graphical abstract and schematic representation were created using Biorender.com. The probability value is indicated as p, where $p < 0.05$ was considered as the statistical level of significance.

Results and discussion

We avoided utilizing any hazardous chemicals and instead employed biocompatible, biodegradable FDA-approved polymer (PLGA) and negligibly immunogenic short nucleotide sequence aptamers to effectively deploy the possible targeted drug delivery in vivo that could lessen its cytotoxicity to healthy tissues by their preferential accumulation in PSMA overexpressed prostate cancer tissue. The following findings were used to substantiate the research envisaged.

Drug–excipients interaction by FTIR analysis

FTIR studies were performed to detect any chemical interactions between the drug molecule and the excipients. The results suggest that (Additional file 1: Figure S1) PLGA showed peaks at 3650 cm^{-1}, 2935 cm^{-1}, and 1735 cm^{-1}, for the O−H stretching, asymmetric stretching of −CH$_2$, and C=O stretching band of the carboxylic acid group, respectively. ABR showed characteristic peaks at 3440 cm^{-1}, 2940 cm^{-1}, 1735 cm^{-1}, 1440 cm^{-1}, 1370 cm^{-1}, and 1250 cm^{-1} for intermolecular bonded O−H stretching vibrations, C−H stretching, C=O stretching, CH$_3$ bending vibration of the acetate group, CH$_3$ bending vibration of the methyl groups and C−O−C stretching vibration of the acetate group, respectively. FTIR spectra of PVA also reveal peaks at 3420 cm^{-1} for intermolecular bonded O−H stretching vibrations, 2925 cm^{-1} for asymmetric stretching of −CH$_2$, and 1740 cm^{-1} due to water absorption. Blank (without drug) nanoparticles (BL-NP) reveal the presence of all characteristic peaks of the polymer PLGA. ABR-NP showed IR peaks at 3490 cm^{-1} due to intermolecular bonded O−H stretching vibrations, 2950 cm^{-1} for C−H stretching, 1760 cm^{-1} for C=O stretching, 1380 cm^{-1} for C−H bending, and 1200 cm^{-1} for C−O stretching due to ester group. Apt-ABR-NP also showed almost similar peaks with one additional peak at 1650 cm^{-1} for C=O stretching due to the amide group. Peaks at 1650 cm^{-1} for Apt-ABR-NP indicated the aptamer binding to the ABR-NPs through amide bond formation. The FTIR study (Additional file 1: Figure S1) indicates no chemical interaction between the ABR and the excipient used in this study. However, a few slight shifts in the peak were solely responsible for the physical interactions that might provide the structure of the formulation. The shift of vibration signals indicated the presence of physical interactions between the compounds for the nanoparticles that might help develop a spherical nanostructure (Dhara et al. 2023).

X-ray photoelectron spectroscopy (XPS)

High-resolution XPS was also used to identify chemical elements and surface chemistry. XPS can provide qualitative and quantitative information on various elements on the particle surface and determine the chemical composition of the uppermost layer of the polymer surface. The XPS spectrum of ABR-NP clearly shows that the O1s peak was at 533 eV and the C1s peak was at 287 eV, confirming the presence of oxygen and carbon elements, respectively, in the PLGA polymer matrix. A very small peak of N1s was observed at 399 eV and appeared in this region with an increasing range. XPS spectra of Apt-ABR-NP nanoparticles showed distinct peaks for oxygen and carbon at 533 and 287 eV, respectively (Fig. 2A). A magnified image of the nitrogen region showed a significant signal at 399 eV, which corresponds to the presence of a large number of N atoms in
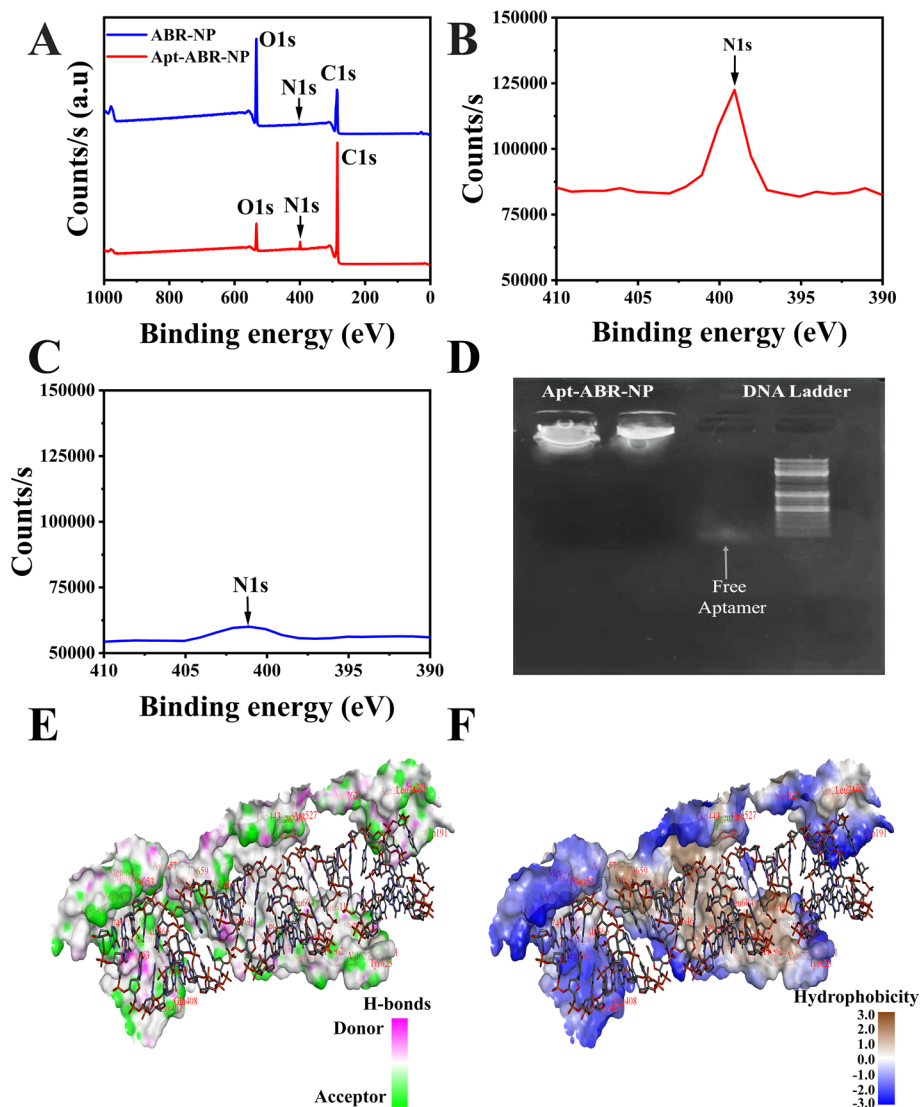
Fig. 2 Aptamer conjugation as assessed by X-ray photoelectron spectroscopy study, and agarose gel electrophoresis, and aptamer–PSMA binding by molecular docking. **A** XPS graph for combined ABR-NP and Apt-ABR-NP, **B** XPS graph for enlarged N1s peak of Apt-ABR-NP, **C** XPS graph for enlarged N1s peak of ABR-NP, **D** aptamer conjugation to ABR-NP using agarose gel electrophoresis, **E** aptamer–PSMA (Protein data bank, PDB: 1Z8L) interactions by hydrogen bonding through molecular docking; **F** aptamer–PSMA (PDB: 1Z8L) hydrophobic interactions through molecular docking

the DNA aptamer. In the XPS spectrum of PLGA nanoparticles, peaks O1 and C1 were located at almost the same binding energy as aptamer-labeled PLGA nanoparticles and PLGA nanoparticles. After the chemical reaction of the PLGA nanoparticles with the aptamer, an amide bond (CO–NH) was formed, which detected a significant N1s peak at a binding energy of 408 eV. For covalent bonds, the higher the polarity, the higher the bond energy. A CO–NH bond was formed here by the conjugation of the aptamer and PLGA-COOH. The presence of nitrogen in the PLGA-aptamer nanoparticles (Apt-ABR-NP) was confirmed using XPS, which observed a higher intensity (Fig. 2B), indicating that the aptamer was successfully conjugated to the PLGA surface because the DNA aptamer contained many nitrogen elements. In contrast, in ABR-NP, only nitrogen

element of the drug molecule, abiraterone acetate was present, resulting in a very small N1s peak (Fig. 2C). This indicates ABR presence on the particle surface also, due to its homogeneous distribution, which was later supported by the findings of HR-TEM. Conjugation of the aptamer to the surface of ABR-NP was successfully confirmed by the XPS plots of the ABR-NP and Apt-ABR-NP. The enlarged plot of aptamer-tagged nanoparticles clearly showed the higher intensity of the nitrogen peak for the abundant presence of the nitrogen atom in the DNA aptamer (Wang et al. 2013).

Aptamer conjugation on the surface of nanoparticles

An agarose gel electrophoresis confirmed that the PSMA-specific DNA aptamer was coupled to the nanoparticle surface. Figure 2D demonstrates that the 32-base pair aptamer moved through the gel and landed parallel to the conventional DNA ladder of the 50-bp marker. The aptamer-coupled nanoparticles (Apt-ABR-NP), on the other hand, stayed inside the loading well, as evidenced by fluorescence. However, the unconjugated nanoparticles (ABR-NP) did not display any band in the well, owing to the lack of a DNA strand. In the instance of Apt-ABR-NP, the image demonstrated the coexistence of DNA aptamer with the nanoparticles, ensuring effective aptamer conjugation on the surface of the nanoparticle, as supported by FTIR data. Further, XPS data support the presence of aptamer on Apt-ABR-NP (Shahriari et al. 2021). Aptamer conjugation to the nanoparticle's surface results in amide bond formation between the carboxylic acid group of the polymer and amine group of the DNA aptamer.

Analysis of aptamer–PSMA interactions by molecular docking

A molecular docking study was performed to check the affinity or interactions between the 32-bp DNA aptamer and prostate-specific membrane antigen (PSMA). Results suggest that nucleotide bases of the aptamer effectively bind with various amino acid residues (Fig. 2E and F). We observed electrostatic interaction between Lysine 406, ARG181, ARG649, and ARG 649 residues and phosphate groups of thymine (DT27), adenine (DA2), adenine (DA11), adenine (DA11), respectively. Several conventional and carbon–hydrogen bonding, along with some hydrophobic interactions, were found between aspartic acid (ASP654), lysine (LYS187), lysine (LYS187), arginine (ARG 190), arginine (ARG649), arginine (ARG190), glutamic acid (GLU748), alanine (ALA635) and methionine (MET663) amino acid residues with adenine (DA2:N3), adenine (DA3:O4'), thymine (DT32:O2), adenine (DA10:O3'), thymine (DT32:O2), thymine (S:DT1), guanine (DG15) and adenine (DA24) nucleotide bases of the aptamer, respectively (Additional file 1: Table S3). The docking score was found to be − 330.86, indicating very good binding affinity between the ligand and receptor. These interactions suggest that aptamer-conjugated nanoparticles can selectively bind to the prostate-specific membrane antigen found in most prostate cancer tissue and the drug molecules reaching the cancer tissues through the targeting method will show its efficacy more efficiently. The DNA aptamer–PSMA binding through molecular docking analysis is also a clear indication of the capabilities of the conjugated nanoparticles to specifically reach PSMA-associated prostate cancer microenvironment.
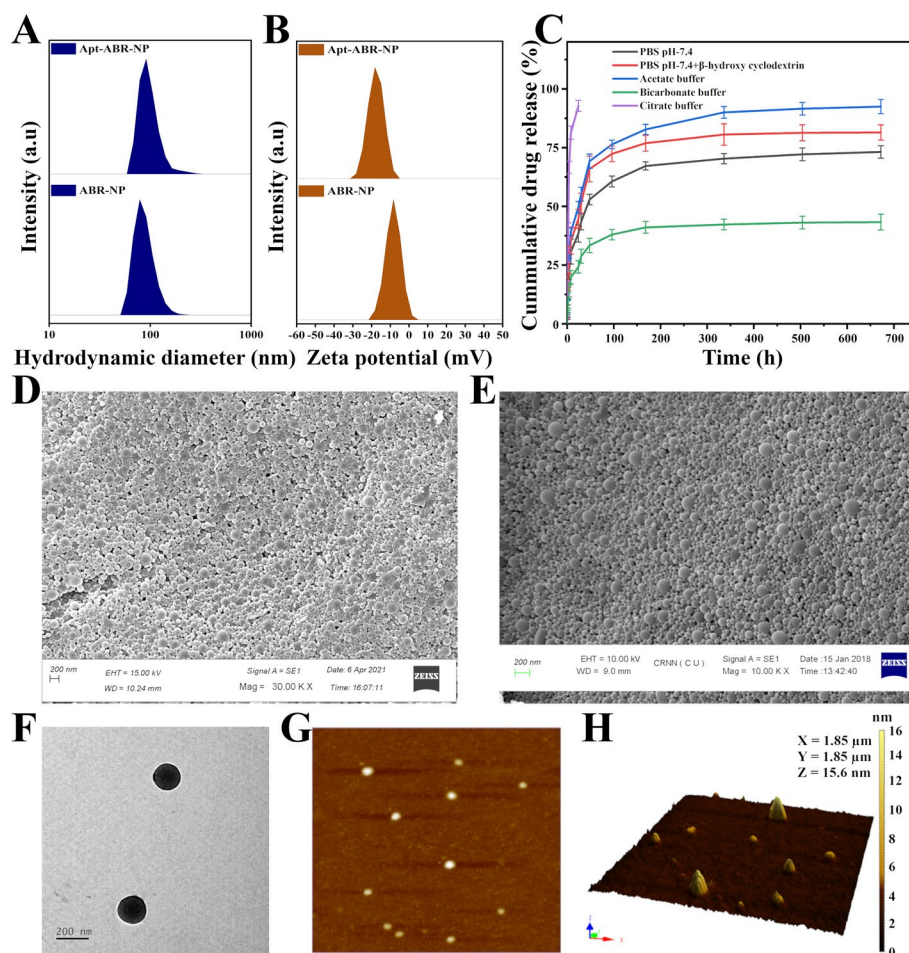
Fig. 3 Determination of particle size, zeta potential, drug release, and electron microscopic imaging and atomic force microscopic evaluation of the experimental nanoparticles. **A** represents particle size distribution of ABR-NP and Apt-ABR-NP, **B** represents zeta potential values of ABR-NP and Apt-ABR-NP, **C** represents in vitro drug release study of Apt-ABR-NP in phosphate buffer saline (PBS pH 7.4), PBS containing 1% β-hydroxy-cyclodextrin, acetate buffer (pH 5), bicarbonate buffer (pH 10) and citrate buffer (pH 3), **D**, **E** represents the FESEM images of ABR-NP and Apt-ABR-NP, respectively, **F** HR-TEM image of Apt-ABR-NP and **G, H** depicts AFM images of Apt-ABR-NP

Determination of particle size and zeta potential

Particle size distribution and zeta potential were measured using the dynamic light scattering method. The average values of the hydrodynamic diameter (d_H) of ABR-NP and Apt-ABR-NP were found to be 130.6 nm and 149.30 nm, respectively (Fig. 3A). However, aptamer conjugation showed approximately 20% enhancement in the size of the ABR-NP. Zeta potential values for ABR-NP and Apt-ABR-NP were − 10.1 mV and − 18.5 mV, respectively (Fig. 3B). The zeta potential values of the nanoparticles imply their stay in a suspended condition in an aqueous medium for a prolonged period. Zeta potential values of nanoparticles greater than ± 30 mV are known to develop more stable suspension (Champion et al. 2007). Thus, the formulations should be stored as a powder that may be suspended in water before administration..

In vitro drug release study

In vitro ABR release from Apt-ABR-NP was carried out in five different media, i.e., phosphate buffer saline (PBS) (pH 7.4), PBS with 1% β-hydroxy cyclodextrin (pH 7.4), citrate buffer (pH 3), acetate buffer (pH 5), and bicarbonate buffer (pH 10), for 28 days (672 h). PBS was chosen as a release medium for its blood environment mimicking pH. The cumulative percentage of drug release after the mentioned time period was found to be 73.12%, 81.45%, 92.76%, 92.45%, and 43.30%, respectively, in 672 h of study in the five different release media (phosphate buffer saline (PBS) (pH 7.4), PBS with 1% β-hydroxy cyclodextrin (pH 7.4), citrate buffer (pH 3), acetate buffer (pH 5), and bicarbonate buffer (pH 10), respectively (Fig. 3C). The drug release data from the nanoparticles were tested on zero-order, first-order, Hixson–Crowell, Korsmeyer–Peppas, and Higuchi kinetic models, and the various regression coefficient values (R^2) for kinetics were tabulated (Additional file 1: Table S2). R^2 values suggest that drug releases, according to Korsmeyer–Peppas, in all five release media.

The drug release in the PBS with β-hydroxy cyclodextrin media showed a biphasic in vitro drug release pattern with an initial fast drug release followed by a sustained drug release pattern for 4 weeks. It could be due to the quick release that drug molecules present on or close to the surface and β-hydroxy cyclodextrin that might help in the better solubility of hydrophobic drug molecules in the drug release medium. ABR release from the nanoparticles followed Korsmeyer–Peppas kinetic, suggesting drug release by diffusion and erosion mechanism (Pattnaik et al. 2012).

The quicker breakdown of the polylactic acid–glycolic acid polymer in citrate buffer (pH 3) than in PBS/PBS with β-hydroxy cyclodextrin explains the faster release pattern of ABR at pH 3. Under the acidic environment (pH 3), the medium promoted the hydrolysis of the PLGA core by attacking ester bonds, resulting in quicker polymer breakdown (Jain et al. 2010). However, at alkaline pH (pH 10), the polymer retains its non-polar character due to the trapping of hydroxyl groups on the polymer surface, which reduces particle water absorption and results in a more stable state of nanoparticles in higher pH environments. The hydrolytic degradation was low to high from neutral, to acidic pH. The quicker drug release pattern in acidic conditions against PBS (pH 7.4) reveals the faster release of ABR from ABR-NP in an acidic tumor environment versus a physiologically neutral medium of blood during their transportation and distribution (Choi et al. 2015).

Surface morphology by FESEM, HR-TEM, and AFM

Drug absorption by cells or organs depends on the surface and shape of the nanoparticle because the nanoparticle surface interacts with the biomembrane, which affects drug internalization (Clogston and Patri 2011; Dutta et al. 2019). Using FESEM, the surface morphology of ABR-NP and Apt-ABR-NP were studied, and photographs of nanoparticles (Fig. 3D, E) revealed that the particle (size 100 nm to 150 nm) were round in shape, with the largest particles measuring 150 nm. Nanoparticles had smooth surfaces with no apparent porosity or fractures. As we did not observe any significant difference in the surface morphologies of the nanoparticles (with and without aptamer conjugation), we further studied the HR-TEM and AFM with the Apt-ABR-NP formulation only. The interior structure of the experimental nanoparticle was studied with high-resolution

transmission electron microscopy (HR-TEM). HR-TEM pictures showed a dark structure (Fig. 3F), indicating that the nanoformulation had a homogeneous drug distribution throughout the particles. The produced nanoparticles had a spherical structure with a smooth surface, as revealed by AFM images (Fig. 3G, H). AFM images in three dimensions showed well-separated nanoparticles within a small size range.

Drug loading and entrapment efficiency

We developed a number of formulations with different drug-to-polymer ratios. Three of these formulations are shown in Additional file 1: Table S1. For each of these three formulations, the amount of drug loaded into the nanoparticles and entrapment efficiencies were calculated. The drug loading percentages for ABR-NP1 and ABR-NP3 were $7.36 \pm 0.5\%$ and $2.61 \pm 0.25\%$, respectively. The highest drug encapsulation was demonstrated by ABR-NP2 (8.5%). As a result, this formulation was chosen as the best one and given the name ABR-NP. This formulation was used for aptamer conjugation. There was a loss of drug during the conjugation process and Apt-ABR-NP had drug loading 8.02%. The ABR-NP encapsulation efficiency was $93 \pm 3.30\%$ and the value was 88.2% in the case of Apt-ABR-NP, demonstrating the method's ability to create nanoparticles with minimum material loss (Dutta et al. 2019).

Stability of the nanoparticles

A stability study of ABR-NP and Apt-ABR-NP revealed that the samples stored at 4–8 °C retained morphology (Fig. 3D, E) and drug content throughout the period. Formulations stored at 30 °C, 75% RH (relative humidity) and 40 °C, 75% RH for 45 and 90 days showed morphological deformation (Additional file 1: Figure S2A, B) and a little decrease in drug content (Additional file 1: Figure S2C). They had morphological deformation during storage at higher temperatures, resulting in enhanced particle size (Additional file 1: Figure S2D). From the stability studies, it was observed that ABR-NP and Apt-ABR-NP were stable at 2–8 °C for up to 90 days (time of investigation). However, the nanoparticles were not stable above 30 °C due to the aggregation of nanoparticles and polymer softening (Yadav and Sawant 2010). Hence, the prepared nanoparticles should be stored at 2–8 °C.

Hydrolytic study

The increase in weight loss upon hydrolytic degradation was used to determine the biodegradability of Apt-ABR-NP. The pH values had a substantial impact on weight loss. The hydrolysis of the formulations increased as the pH of the medium was reduced. After a 4-week investigation, mass loss was $11.23 \pm 2.14\%$ at pH 10, $20.73 \pm 1.41\%$ at pH 7.4, $30.83 \pm 1.98\%$ at pH 5, and $48.26 \pm 2.61\%$ at pH 3, respectively (Additional file 1: Figure S2E). The results indicated that our nanoformulation was more stable in phosphate buffer (pH 7.4) and bicarbonate buffer (pH 10), as compared to citrate (pH 3) and acetate buffer (pH 5). The findings suggest that the faster drug release would occur as the Apt-ABR-NP reaches acidic tumor microenvironment.
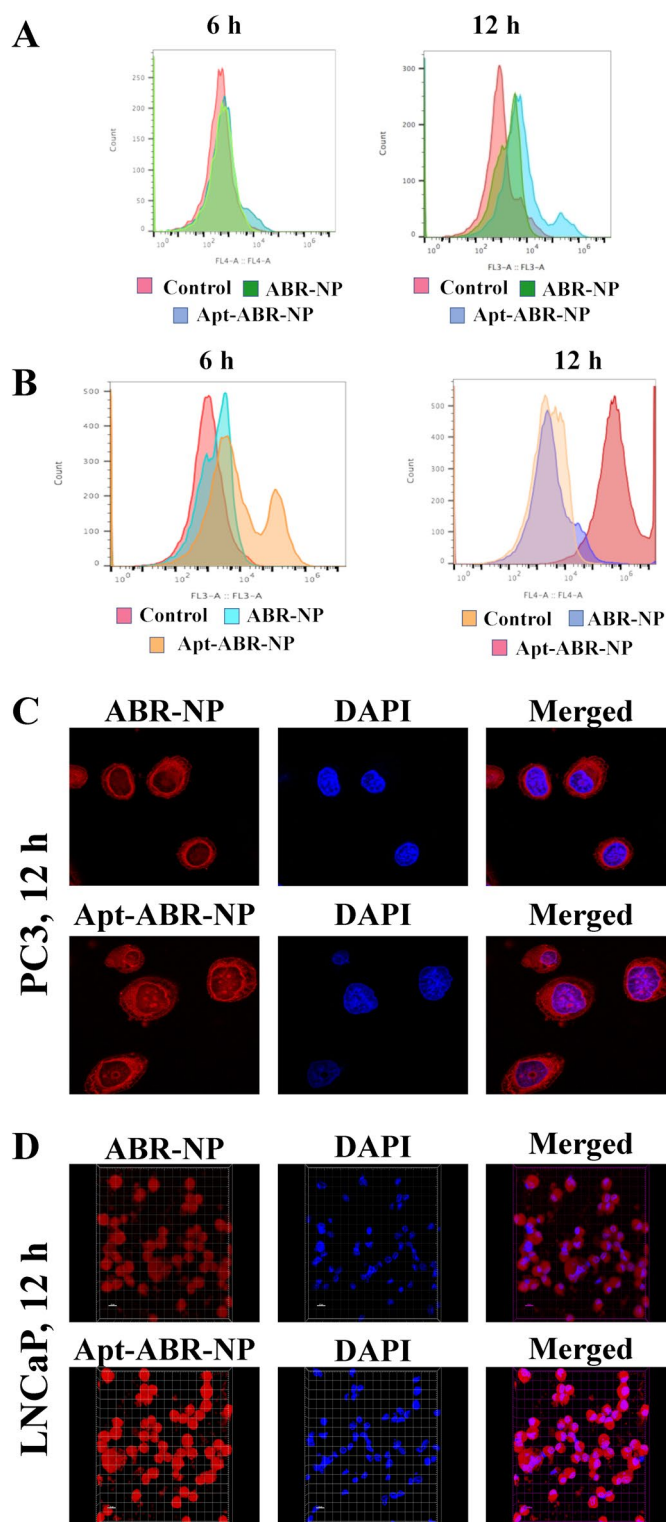
Fig. 4 Cellular uptake study. **A** FACS histogram PC3 cells after the treatment with ABR-NP and Apt-ABR-NP at 6 h and 12 h. **B** FACS histogram LNCaP cells after the treatment with ABR-NP and Apt-ABR-NP at 6 h and 12 h. **C** Confocal laser microscopy images of PC3 cells at 12 h after the treatment with ABR-NP and Apt-ABR-NP. **D** Confocal laser microscopic images of LNCaP cells at 12 h after the treatment with ABR-NP and Apt-ABR-NP

In vitro cellular uptake analysis by flow cytometry and confocal microscopy

Flow cytometry analysis revealed a time-dependent gradual accumulation of Apt-ABR-NP in both PC3 (Fig. 4A) and LNCaP (Fig. 4B) cells. In the case of PC3 cells, an inadequate percentage of nanoparticle uptake was observed from 6 to 12 h of treatment. However, in the case of LNCaP cells, longer incubation with nanoparticles significantly enhanced cellular uptake, especially for Apt-ABR-NP. This could be due the fact that LNCaP cells overexpress the surface antigen PSMA, whereas PC3 cells are PSMA negative. The Apt-ABR-NP fluorescent intensity was highest for 12 h of treatment in the case of LNCaP cells suggesting the PSMA-specific strong binding affinity of aptamer functionalized nanoparticles with LNCaP cell-surface biomarker for prostate cancer. Furthermore, to validate targeting specificity of the nanoparticle surface conjugated aptamer against PSMA receptor, we performed cellular uptake study on 22Rv1. As expected, enhanced cellular internalization was observed for PSMA-targeted nanoparticles.

We further compared the cellular internalization of ABR-NP and Apt-ABR-NP nanoparticles at 12 h confocal microscopy for PC3 and LNCaP cells. Corresponding images reflected nanoparticles accumulation inside the cytoplasm of PC3 (Fig. 4C) and LNCaP cells (Fig. 4D) with the progression over time. However, comparatively higher accumulation was found in the case of LNCaP cells, as represented by red fluorescence intensity confirming the intense binding specificity of aptamer with PSMA, which facilitated the higher accumulation of Apt-ABR-NP in LNCaP cells, especially with a longer incubation period.

The cellular uptake study using flow cytometry analysis was also conducted on 22Rv1 prostate cancer cells that overexpress PSMA and are AR positive also. The data showed the time-dependent increase of the uptake of ABR-NP and Apt-ABR-NP in 22Rv1 cells (Fig. 5A). However, the cellular uptake was more in the case of Apt-ABR-NP.
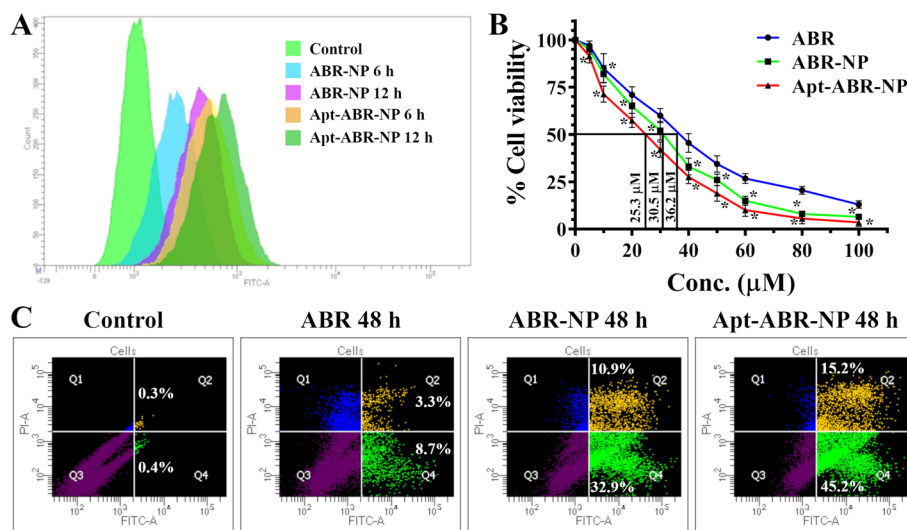

Fig. 5 In vitro evaluation of cellular uptake, cytotoxicity, and apoptosis in 22Rv1 cells. **A** FACS histogram for cellular uptake measurement after the treatment with ABR-NP and Apt-ABR-NP at 6 h and 12 h. **B** IC_{50} values of ABR, ABR-NP, and Apt-ABR-NP on 22Rv1 cells (data show mean ± SD, $n = 3$; * indicates $p < 0.05$ when compared against ABR- treated group of mice), and **C** induction of apoptosis in 22Rv1 cells after treatment with ABR, ABR-NP, and Apt-ABR-NP for 48 h

Many reports are available regarding cellular internalization aptamer-conjugated PLGA nanoparticles. Aptamer-conjugated PLGA nanoparticles have been reported to internalize into the cells by receptor-mediated endocytosis and micropinocytosis (Liu et al. 2009; Shishparenok et al. 2023; Wan et al. 2019; Yallapu et al. 2014). The aptamer of Apt-ABR-NP interacts with the PSMA in clathrin-dependent endocytosis by forming clathrin-coated pits. The clathrin coat detaches and aptamer-conjugated formulations are internalized in endosomes and lysosomes before their distribution to other cellular organelles (Shishparenok et al. 2023; Wan et al. 2019). Caveolar-mediated endocytosis of aptamer conjugated formulations after aptamer–PSMA interactions entails the development of caveolae vesicles mediated through dynamins found in caveolae (Shishparenok et al. 2023; Wan et al. 2019). Aptamers move over the membrane to the caveolae after binding to the targeted surface membrane antigen, PSMA.

Apt-ABR-NP may be endocytosed by clathrin and caveolae-dependent and caveolae-independent pathways (Yallapu et al. 2014). Hence, multiple receptor-mediated endocytotic pathways were involved in the aptamer-conjugated formulations (Liu et al. 2009).

Rapid endolysosomal escape of PLGA nanoparticles into the cytosol due to selective reversal of surface charge of PLGA nanoparticles from anionic to cationic in the acidic
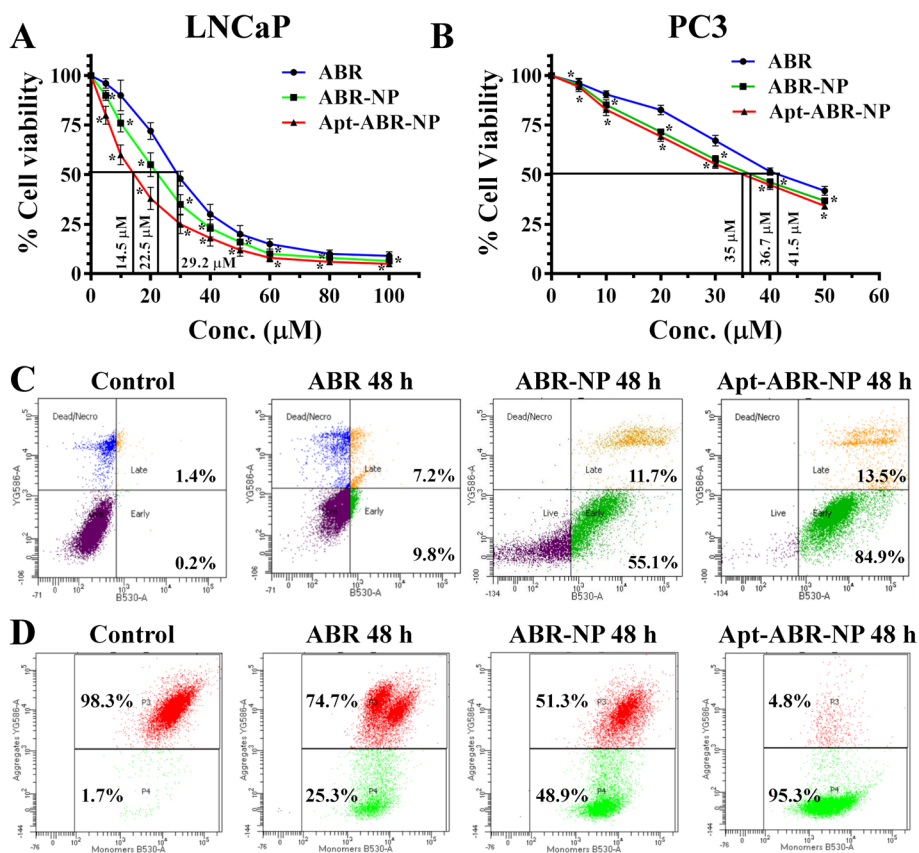

Fig. 6 Cell cytotoxicity, apoptosis, and mitochondrial membrane depolarization assay of ABR, ABR-NP, and Apt-ABR-NP evaluated in vitro. **A** IC_{50} values of ABR, ABR-NP, and Apt-ABR-NP on LNCaP and **B** PC3 cells after 48 h of treatment (data show mean ± SD, $n = 3$; * indicates $p < 0.05$ when compared with ABR-treated group of mice). **C** Induction of apoptosis in LNCaP cells after treatment with ABR, ABR-NP, and Apt-ABR-NP for 48 h. **D** Mitochondrial membrane depolarization after 48 h of treatment, with ABR, ABR-NP, and Apt-ABR-NP for 48 h

endolysosomal environment is a well-established mechanism for lysosomal escape of PLGA nanoparticles (Panyam et al. 2002).

In vitro cytotoxicity assay

The percentage viability data of 22Rv1, LNCaP, and PC3 cells, which received the treatment of the free drug and the experimental nanoparticles are represented in Figs. 5B, 6A, and B, respectively. Apt-ABR-NP had the highest cytotoxicity on LNCaP cells (lowest IC_{50} value 14.5 ± 1.2 µM) followed by 22Rv1(IC_{50} value 25.3 ± 1.1 µM) compared to ABR and ABR-NP. ABR showed an IC_{50} of 29.2 ± 3.1 µM, while ABR-NP showed the value of 22.5 ± 2.6 µM in LNCaP cells. Significant reduction of the IC_{50} value was observed for both of the nanoparticles (ABR-NP and Apt-ABR-NP) on LNCaP cells, representing their enhanced therapeutic efficacy in comparison to free ABR. On the contrary, the cytotoxicity of ABR and its formulations on PC3 cells was comparatively lower than on LNCaP cells. The IC_{50} values on PC3 cells were found to be 41.5 ± 2.4 µM, 36.7 ± 1.6 µM, and 35 ± 2.0 µM for ABR, ABR-NP, and Apt-ABR-NP treatments, respectively. All the cytotoxicity assay data suggest that ABR-NP and Apt-ABR-NP demonstrated enhanced therapeutic potency on LNCaP cells. The cytotoxic effect of ABR-NP and Apt-ABR-NP in PSMA-positive prostate cancer LNCaP cells and PSMA-negative prostate cancer PC3 cells showed that the highest dose reduction was in Apt-ABR-NP treated LNCaP cells. However, PC3 cells were less sensitive to ABR, ABR-NP, and Apt-ABR-NP, as PSMA-negative PC3 cells are also androgen insensitive in nature and ABR functions by inhibiting androgen production (Bouhajib and Tayab 2019; Mukherjee and Mayer 2008). The aptamer conjugation decreased the IC_{50} value by 51% in PSMA-positive LNCaP cells. The findings fairly matched the earlier reports by Fernanda da Luz Efe. 2019, and Pokrovsky et al. 2020 (Pokrovsky et al. 2020; Wang et al. 2019). The investigation suggests that PSMA binding and inhibition of androgen production had predominant role in the cellular internalization and cellular function mediated through Apt-ABR-NP. Hence, we proceeded with further in vitro studies on LNCaP cells.

Apoptosis assay

Apoptosis is a programmed cell death, and most anticancer agents are expected to have an apoptosis-inducing capacity (Diepstraten et al. 2022). The apoptosis-inducing potential of ABR, ABR-NP, and Apt-ABR-NP through the Annexin V-FITC/PI dual staining method demonstrated the superior apoptosis-inducing ability of Apt-ABR-NP, suggesting its applicability as a potential chemotherapeutic formulation.

The total apoptotic population in 22Rv1 cells after treatment with ABR for 48 h was 12% (8.7% early and 3.3% late apoptosis) (Fig. 5C). ABR-NP treatment increased apoptosis to 43.8% (32.9% early and 10.9% late apoptosis) and Apt-ABR-NP treatment showed the value 60.4% (45.2% early and 15.2% late apoptosis) in 22Rv1 cells.

Figure 6C demonstrates apoptosis on LNCaP cells. The total apoptotic population after treatment with ABR for 48 h was 17% (9.8% early and 7.2% late apoptosis), which was increased up to 66.8% (55.1% early and 11.7% late apoptosis) and 98.4% (84.9% early and 13.5% late apoptosis) in the cases of ABR-NP and Apt-ABR-NP treatments, respectively. We found highest percentage of apoptotic cell death for Apt-ABR-NP as compared to ABR and ABR-NP after 48 h of incubation in LNCaP cells. On an overall comparison,

Apt-ABR-NP-induced apoptosis was higher at all the incubation time points than free drug, ABR, and unconjugated nanoparticles ABR-NP. Thus, Apt-ABR-NP is a potential cytotoxic candidate against PSMA-positive prostate cancer LNCaP cells compared to ABR and ABR-NP.

Mitochondrial membrane depolarization analysis using JC-1

Mitochondrial membrane depolarization is a signature characteristic of apoptosis, and this can be measured using JC-1 staining (Li et al. 2022). JC-1 is a sensitive marker for mitochondrial membrane potential that accumulates in the mitochondria in a potential-dependent manner. JC-1 forms J-aggregates at high mitochondrial membrane potential, emitting red fluorescence, whereas at low mitochondrial membrane potential, JC-1 remains monomer, emitting green fluorescence. The JC-1 ratio (an indicator of the J-aggregates/monomers ratio) is used to quantify mitochondrial health and activity. An increase in the JC-1 monomer:aggregate ratio (that is, green:red fluorescence intensity) detects an increase in the apoptotic population. In our experiment, the free drug ABR showed a change of green fluorescence to 25.3% after 48 h of treatment. In the case of ABR-NP, the percentage of JC-1 monomer was found to be 48.9% at 48 h of treatment. Cell population with depolarized mitochondria (indicated by green fluorescence) was further increased to 95.3% in the case of Apt-ABR-NP treatment at 48 h (Fig. 6D). The higher cell population with depolarized mitochondria after Apt-ABR-NP treatment represents its potency in higher apoptosis of LNCaP cells compared to ABR or ABR-NP. This finding also correlates well with the outcome of the apoptosis assay.

In vitro colony formation assay

Figure 7A shows the representative images of the wells after crystal violet staining of control and the treatment groups ABR, ABR-NP, or Apt-ABR-NP on LNCaP cells. The number and size of the growth of the colonies were found to be reduced in the highest
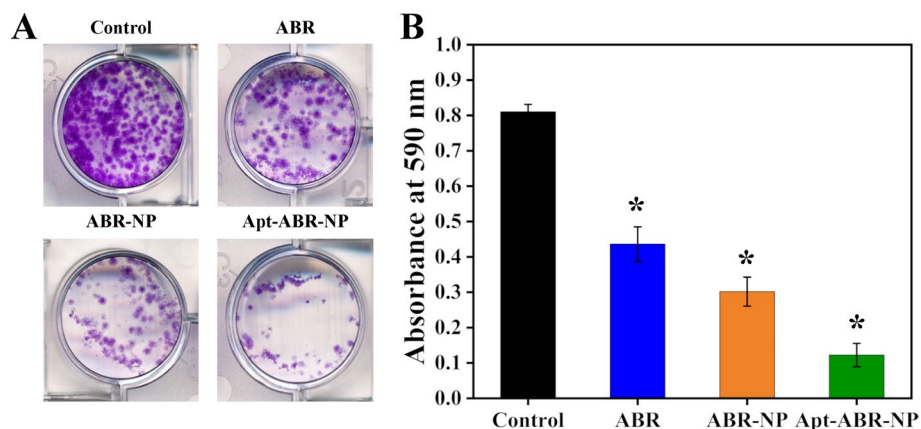

Fig. 7 Clonogenic assay with LNCaP cells using ABR, ABR-NP, and Apt-ABR-NP. **A** More growth in untreated (control) was followed by ABR, ABR-NP, or Apt-ABR-NP treated LNCaP cells. **B** Absorbance values of untreated (control) and ABR, ABR-NP, or Apt-ABR-NP treated LNCaP cells, after crystal violet staining, represent the colonies' density. Values represent mean $\pm$ SD ($n = 3$), where * indicates $p < 0.05$ is the statistical level of significance, compared against the control value as assessed by Student's *t*-test
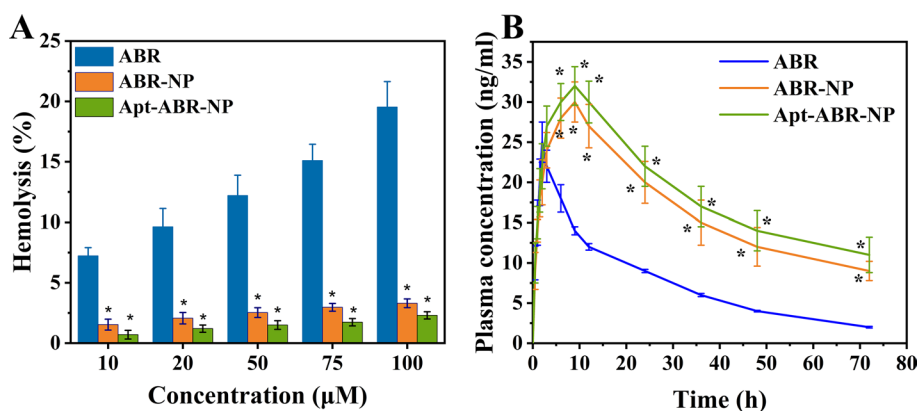
Fig. 8 Hemolytic activity and pharmacokinetic profile of ABR, ABR-NP, and Apt-ABR-NP. **A** Hemolytic activity of ABR, ABR-NP, and Apt-ABR-NP was measured by incubating each sample with red blood cells and measuring the amount of hemoglobin released. The percentage of hemolysis was plotted against the concentration of the samples. Data show mean $\pm$ SD ($n=3$) where $p<0.05$ is the statistical level of significance as assessed by Dunnett's test (compared against control group). **B** The pharmacokinetic profile of ABR, ABR-NP, and Apt-ABR-NP was assessed in mice by measuring the concentration of ABR from each sample in the bloodstream over time. The data were plotted as the mean concentration of each sample at each time point. Error bars indicate standard deviation ($n=3$). *Marks represent significant values ($p<0.05$) when ABR-NP and Apt-ABR-NP were compared with ABR through the two-way ANOVA test, and the statistical significance of data was analyzed through Bonferroni's post-test

Table 1 Pharmacokinetic parameters of ABR, ABR-NP, and Apt-ABR-NP in Swiss Albino mice following intraperitoneal administration (0.4 mg/kg)

Parameters	ABR	ABR-NP	Apt-ABR-NP
C_{max} (ng/ml)	25 $\pm$ 2.5	30 $\pm$ 2.5*	32 $\pm$ 2.4*
T_{max} (h)	2.0 $\pm$ 0.2	9.0 $\pm$ 0.4*	9.0 $\pm$ 0.5*
AUC last (ng h/ml)	547 $\pm$ 27	1204 $\pm$ 167*	1356 $\pm$ 175*
AUC 0–∞ (ng h/ml)	582 $\pm$ 30	1672 $\pm$ 175*	1975 $\pm$ 194*
AUMC (ng h^2/ml)	12,345 $\pm$ 416	34,325 $\pm$ 544*	39,603 $\pm$ 622*
$T_{1/2}$ (h)	12 $\pm$ 0.4	36 $\pm$ 1.7*	39 $\pm$ 2.2*
MRT (h)	22.5 $\pm$ 1.1	28.5 $\pm$ 1.6*	29.2 $\pm$ 1.2*
V_d (ml)	316 $\pm$ 10	430 $\pm$ 12*	415 $\pm$ 20*
Clearance (ml/h)	18.2 $\pm$ 0.9	8.3 $\pm$ 0.8*	7.4 $\pm$ 0.2*

Data show mean $\pm$ SD ($n=3$). Statistical analysis was carried out to one-way ANOVA analysis, and the p-value was calculated through Tukey's post-test ($p<0.05$) when compared against ABR control. Data shown by star (*) were significant compared to the ABR control group

percentage in the case of Apt-ABR-NP treated cells. The absorbance values of the individual wells taken at 590 nm are shown for quantitative comparison (Fig. 7B).

Different therapeutic approaches, such as free drug (ABR), nanoparticulated forms, ABR-NP, and Apt-ABR-NP, inhibited cellular growth. The maximum therapeutic efficacy was observed in the case of Apt-ABR-NP. All the in vitro assays represented the highest anti-proliferative activity in the case of Apt-ABR-NP, which can well correlate with aptamer–PSMA binding mediated accumulation of Apt-ABR-NP in prostate cancer cells.

Hemolysis study

The drug (ABR) and different nanoformulations (ABR-NP and Apt-ABR-NP) were tested for hemocompatibility in a range of concentration levels (10 to 100 μM) (Fig. 8A). The results revealed that the formulations (ABR-NP and Apt-ABR-NP) had low hemolytic activity (< 5%) as compared to that of free ABR at varying concentration levels. The study showed that the tested dose range for both the nanoformulations had low hemolytic activity and may be safely used for intravenous delivery. One of the most important requirements for the effective in vivo application of blood-contacting biomaterials is their hemocompatibility (Krishnan et al. 2023). The hemocompatibility study suggests that the nanoformulations exhibited modest hemolytic activity and were safe for intravenous administration.

Pharmacokinetics study

In vivo pharmacokinetic profiles of ABR, ABR-NP, and Apt-ABR-NP were assessed in Swiss albino mice. Table 1 represents the pharmacokinetic parameters (AUC, C_{max}, T_{max}, AUMC, $T_{1/2}$, MRT, V_d, *CL*) of ABR, ABR-NP, and Apt-ABR-NP following intraperitoneal injection in Swiss Albino mice (Dutta et al. 2018). ABR (abiraterone acetate) becomes converted into abiraterone (ART) rapidly when it comes in contact with blood plasma, hence reaching a high concentration ($C_{max} = 25 \pm 2.5$ ng/ml) of ART within a short time (T_{max}, 2 h) (Fig. 8B). On the other hand, both ABR-NP and Apt-ABR-NP maintained a sustained plasma concentration of ART for a long time (around 24 h). In the case of ABR-NP and Apt-ABR-NP, C_{max} was reached at around 9 h of injection, followed by a slow elimination phase, suggesting sustained release characteristics of both formulations. The AUC was increased by 2.2 times and 2.47 times in the case of ABR-NP and Apt-ABR-NP, respectively, compared to the free drug (ABR). The half-life of the active drug (ART) was increased significantly by 3 times and 3.25 times for ABR-NP and Apt-ABR-NP, respectively. AUMC and MRT were subsequently increased for both formulations compared to the free drug (ABR). Data suggest an increased bioavailability of the active drug while delivered through nanoparticle formulations. The nanoencapsulation

Table 2 Biodistribution of ^{99m}Tc-ABR-NP and ^{99m}Tc-Apt-ABR-NP in testosterone/MNU-induced prostate cancer-bearing mice

Organ/tissue	%ID of ^{99m}Tc-ABR-NP in CRPC mice			%ID of ^{99m}Tc-Apt-ABR-NP in CRPC mice		
	1 h	2 h	5 h	1 h	2 h	5 h
Blood[#]	3.882 ± 0.01	3.601 ± 0.22	3.228 ± 0.28	4.156 ± 0.31	3.946 ± 0.31	3.644 ± 0.42
Heart	0.545 ± 0.12	0.602 ± 0.05	0.664 ± 0.04	0.712 ± 0.03	0.722 ± 0.07	0.730 ± 0.04
Liver	20.12 ± 2.10*	24.55 ± 2.00*	22.44 ± 4.34*	23.60 ± 2.55*	26.04 ± 2.01*	30.58 ± 1.80*
Lungs	0.563 ± 0.21	0.578 ± 0.23	0.606 ± 0.32	0.688 ± 0.20	0.894 ± 0.20	1.142 ± 0.33
Stomach	0.448 ± 0.16	0.382 ± 0.10	0.404 ± 0.11	0.725 ± 0.10	0.784 ± 0.11	0.942 ± 0.20
Intestine	2.762 ± 0.51	2.920 ± 0.31	3.752 ± 0.30	3.114 ± 0.12	3.205 ± 0.55	4.025 ± 0.62
Kidney	3.452 ± 0.30	4.348 ± 0.42	7.88 ± 0.528*	4.565 ± 0.45*	7.14 ± 0.642*	10.24 ± 0.47*
Prostate	1.642 ± 0.21	1.811 ± 0.16*	2.313 ± 0.22*	2.256 ± 0.30	2.622 ± 0.24*	3.142 ± 0.36*
Urine	26.56 ± 3.89*	30.56 ± 2.18*	32.44 ± 2.14*	30.12 ± 1.55*	33.56 ± 2.51*	37.12 ± 3.18*

[#] Represents %ID/g in the case of blood, otherwise %ID in the whole organ

*Marks represent statistically significant values when both ^{99m}Tc-ABR-NP and ^{99m}Tc-Apt-ABR-NP were compared for different time points in two-way ANOVA analysis and tested by Bonferroni's post-test ($p < 0.05$)

of ABR maintained a sustained plasma concentration of ART compared to free-drug treatment. Sustained drug release and predominantly slower elimination of the drug from the nanoparticle caused enhanced plasma half-life of the drug. The overall observation suggests that Apt-ABR-NP had a better pharmacokinetic profile among the experimental formulations for ABR therapy. Aptamer-conjugation on the surface might have improved the aqueous microenvironment on the nanoparticle surface, which might deter drug release further to provide a more sustained drug release profile and improve the pharmacokinetic parameters for Apt-ABR-NP studied here.

Biodistribution study and gamma-scintigraphy imaging

The distribution of ^{99m}Tc-radiolabeled nanoparticles in different organs of prostate cancer-bearing Swiss Albino mice is mentioned in Table 2. Data suggest that nanoparticles remained in the blood for a longer time in blood circulation. In contrast, the free drug (ABR) was eliminated rapidly. The majority of the radiolabeled nanoparticles was eliminated through urine. ^{99m}Tc-ABR-NP and ^{99m}Tc-Apt-ABR-NP accumulated significantly in the liver, which is common in the nanoparticulated drug delivery system due to the
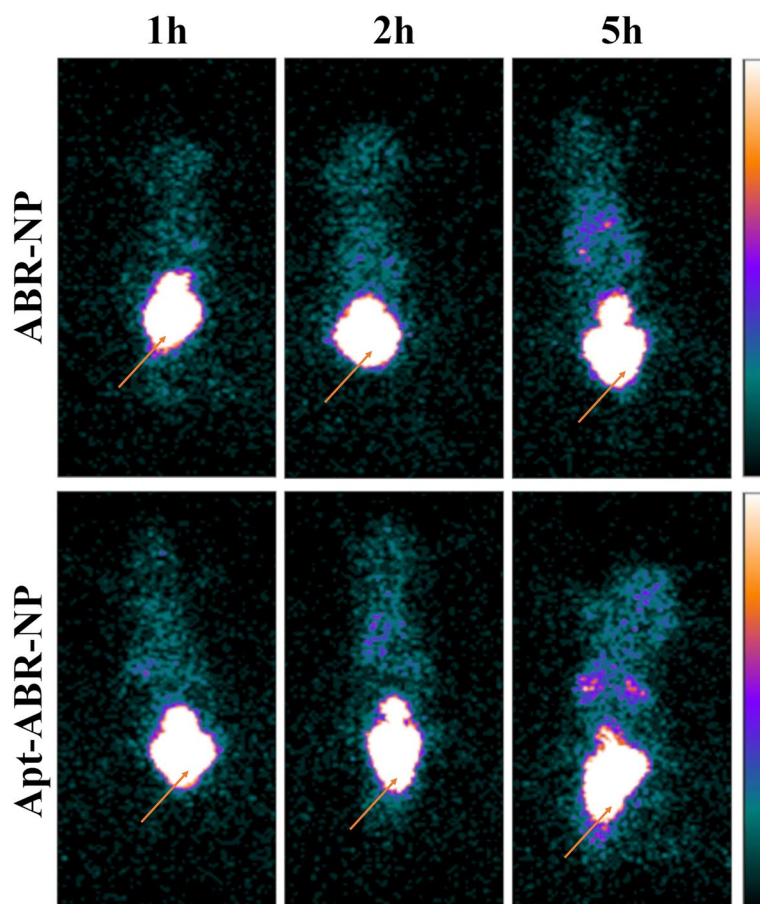

Fig. 9 Biodistribution study of radiolabelled nanoparticles in various organs using gamma scintigraphic imaging. Radiolabelled nanoparticles (^{99m}Tc-ABR-NP and ^{99m}TcApt-ABR-NP) were injected into mice via tail vein, and gamma scintigraphic images were acquired at different time points (1, 2, and 5 h post-injection) using a gamma camera. Arrows indicate the prostate region in the mice

reticuloendothelial entrapment system (RES) of the liver (Yang et al. 2022). Apart from the liver, the accumulation of nanoparticles in the kidney and intestine was also considerable. Accumulation of ^{99m}Tc-Apt-ABR-NP in our target organ prostate was much higher than ^{99m}Tc-ABR-NP in a time-dependent manner (e.g., 3.14% vs. 2.25% at 5 h), suggesting enhanced tumor uptake for aptamer conjugated prostate cancer therapy.

Gamma-scintigraphy images (Fig. 9) revealed deposition of Apt-ABR-NP in the prostate region with the progress of post-injection time. Although urine contained most radioactivity and the bladder covers a wide region, distinguishing the prostate from the bladder was difficult in the scintigraphy images. Signals from other organs, such as the liver, kidney, lungs, intestine, etc., were correlated well with quantitative measurements obtained from the biodistribution study. Gamma-scintigraphy imaging of the prostate cancer animal model following injection of radiolabeled nanoparticles provided in vivo
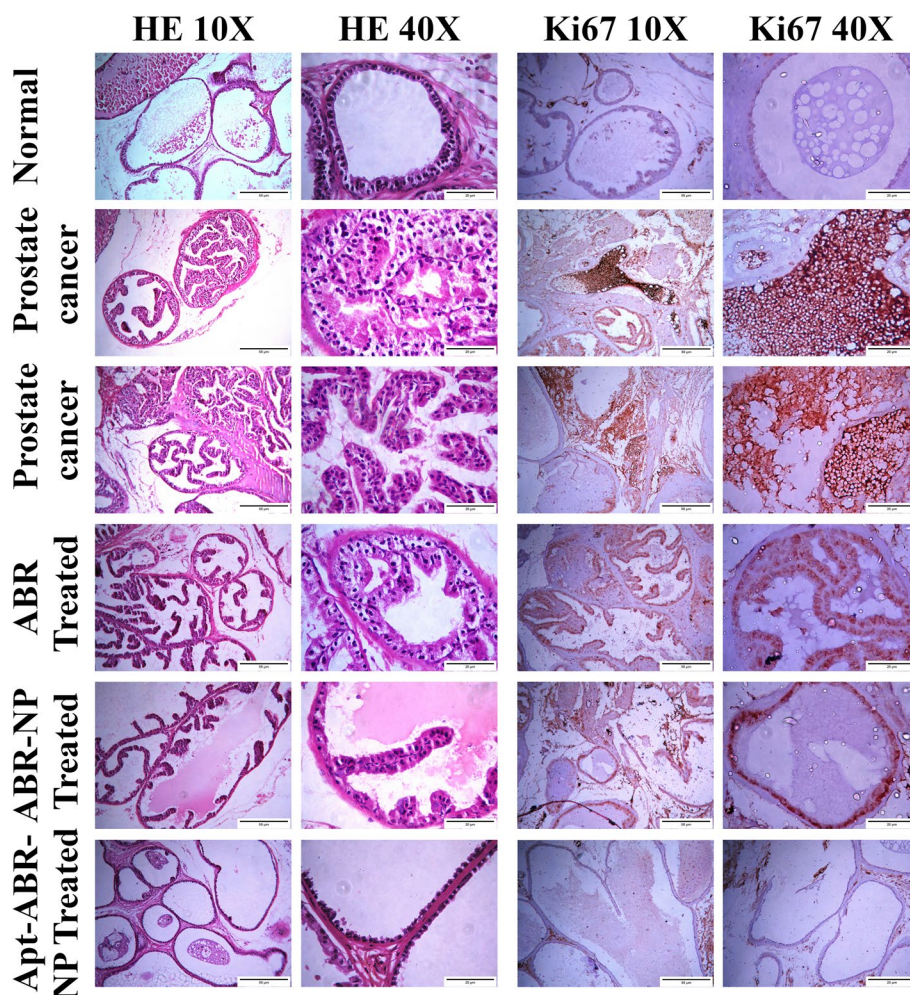

Fig. 10 Antitumor efficacy of ABR, ABR-NP, and Apt-ABR-NP in prostate cancer (PCa) tissues. Histological examination of prostate cancer tissues and normal prostate tissues was performed using hematoxylin and eosin (HE) staining. Representative images of prostate cancer tissues and normal prostate tissues are shown. The expression of Ki67, a marker of cell proliferation, in prostate cancer tissues and in the normal prostate tissue sections were analyzed by immunohistochemistry. The staining/immunohistochemistry and magnification of the photographs done are mentioned above each column

assessment of experimentally generated nanoparticles (Yin et al. 2017). Radiolabeled PSMA-targeted Apt-ABR-NP signaling was observed to increase the prostate and surrounding area in experimental mice with prostate cancer in a time-dependent manner, ensuring the target specificity of conjugated aptamer toward prostate cancer (Hazra et al. 2021; Shah et al. 2021).

Antitumor activity study

The microscopic images of normal mouse prostate sections showed the glandular structure of the prostate gland lined with cuboidal epithelial cells arranged in a distinct convoluted pattern (Fig. 10, panel 'Normal'). The lumen of the glands was lined with cuboidal epithelial cells with small nuclei, and the stroma consisted of a thin fibromuscular matrix containing blood vessels and poorly defined smooth muscles. In the 'carcinogen with testosterone'-treated prostate cancer group (panel cancer), the epithelial cells of the glands were transformed into large columnar-like cells that caused shrinkage of the lumen, increased the scalloping of the lumen, and created large intraglandular vacuoles. The thickness of the stroma was increased. Fibromuscular striation was formed in the stroma, representing stromal atrophy (Fig. 10, panel 'Cancer'). In the prostates of 'Cancer' group, glandular hyperplasia and nuclear atypia (large nucleus with distinctively prominent nucleolus) were also observed. According to the Gleason grading system (Munjal and Leslie 2023), the cancers of the MNU with testosterone-treated prostates were found to have pattern 3 carcinomas (i.e., they have recognizable glands with small number of infiltrating invasive cells in the surrounding tissues) and pattern 4 carcinomas (i.e., they have recognizable, glomeruloid glands with a large number of invasive cells in the surrounding tissues forming neoplastic clumps). Hence, they were considered to have either Gleason 7 or Gleason 8 score representing a moderately differentiated to poorly differentiated carcinoma. Treatment with ABR and its formulations ameliorated the prostate's morphological atrophy caused by MNU and testosterone. Treatment with ABR improved the stromal fibromuscular structure but did not completely restore the epithelial convolution pattern similar to the normal prostate. The Gleason grading system of the ABR-treated prostates showed pattern 2 carcinomas (i.e., they have loosely arranged oval-shaped glands with minimal invasion) and pattern 1 carcinoma (i.e., they are very similar to normal prostate tissues with closely packed glands), which gives a Gleason score of 2 or 3 in this case. This represented that treatment with ABR ameliorated the invasiveness of the cancer tissues and helped in restoration of tissue architecture. Treatment with ABR-NP and Apt-ABR-NP further reduced stromal atrophy and restored the epithelial lining convolution comparable to the normal prostate. In ABR-NP and Apt-ABR-NP treated groups, prostate morphology was very similar to normal prostates and Gleason scoring was not determinable. On overall observation, Apt-ABR-NP performed much better in restoring the overall morphological structure of carcinogen with testosterone-treated prostate carcinogenesis group compared to those of ABR and ABR-NP treated groups of animals.

Ki67 is a cell proliferative marker and is considered one of the most important immunohistochemical biomarkers for tumor prognosis (Berlin et al. 2017). Although the grading system in prostate cancer is primarily based on tissue architecture and does not consider the proliferation rate of cells (which is common in grading of many

other cancer), but Ki67 staining provides significant correlation in the clinical estimation of disease prognosis through needle biopsies, transurethral resections, and prostatectomy. In our study, we used Ki67 immunohistochemical staining of mouse prostates to identify any prognostic correlation between the percentage of proliferating cells and disease stage, with or without treatment of ABR and its formulations. The Ki67 staining of 'Normal' prostates showed $\leq 3\%$ Ki67(+) cells and was considered as negative (Fig. 10, panel 'Normal'). Prostates from MNU + testosterone treated groups (Fig. 10, the 'Cancer' groups) showed 30–50% Ki67(+) cells (counted in areas with $40 \times$ magnifications) and the Gleason score was considered as 2+. In combination with Gleason scores 7 and 8, they represent moderate to poorly differentiated carcinomas with an intermediate proliferation rate. Treatment with ABR, ABR-NP, and Apt-ABR-NP in carcinogenic mice reduced the population of Ki67(+) cells to $15 \pm 2\%$, $10 \pm 2\%$, and $5 \pm 1.5\%$, respectively (representative images are shown in Fig. 10, panels 'ABR', 'ABR-NP', and 'Apt-ABR-NP'). This represented ABR and its nanoformulations significantly reduced invasiveness of prostate tumors, and this effect was highest in the case of Apt-ABR-NP. Combined analysis of morphological restoration, inhibition of stromal degeneration, and proliferation-inhibition suggests that Apt-ABR-NP could be a good candidate to treat hormone-resistant prostate adenocarcinoma. The findings demand further investigations on it.

Efficacy of Apt-ABR-NP on LNCaP tumor spheroid model

To support the findings of carcinogen-induced prostate cancer mouse model in a more informative and conclusive manner, an additional pharmacodynamic experiment was performed on LNCaP 3D tumor spheroid model. Tumor spheroid is a 3D model with accurate physicochemical environment that is comparable to in vivo conditions (Adamiecki et al. 2022; Volpatti and Yetisen 2014).

Cy5-loaded Apt-ABR-NP formulation was used in its IC_{50} dose on two approximately equal size of LNCaP tumor spheroids. The spheroid was treated with Apt-ABR-NP for once in a day for 3 consecutive days. After 72 h Apt-ABR-NP-treated spheroid reduced its size by nearly 60% (Additional file 1: Figure S3). Cancer control spheroid (without treatment) showed the expression of the DAPI throughout the body, whereas DAPI expression was more peripheral for the Apt-ABR-NP treated spheroid, suggesting less live proliferative cells compared to the cancer control spheroid. Thus the experiment showed predominant role of the Apt-ABR-NP in reducing LNCaP cell tumor.

Hematological evaluation

The CBC profile and CRP level of animals from different groups (A–F) are represented in Additional file 1: Table S4. In the case of "Cancer" control group (Group B), lower RBC count and higher WBC count were observed than normal animals. Lowered lymphocyte count and enhanced neutrophil count were also noticed as a mark of higher inflammatory activities in cancer-bearing animals (Group B). Treatment with ABR, ABR-NP, and Apt-ABR-NP treatment increased blood lymphocyte

count and reduced neutrophil count compared to "Cancer" group, suggesting better immunogenic response to treatment. The "Cancer" group of animals also showed a lower platelet count compared to "Normal" group animals. No significant changes were observed in hematocrit volume and hemoglobin content after treatment with ABR, ABR-NP, and Apt-NP in normal mice. Overall observation suggests that treatment with ABR, ABR-NP, and Apt-ABR-NP reduced inflammatory response element (CRP), increased immunogenic response, and subsequently tried to restore CBC profile close to normal. Upon treatment of normal animals with best represented formulation, Apt-ABR-NP (Group F), no significant anomaly was observed in CBC profile, suggesting its biocompatible and non-hemotoxic nature. PSMA analysis showed a high amount of PSMA in blood in cancer-bearing animals (25 ± 1.6 ng/ml) compared to normal animals (5.2 ± 0.6 ng/ml). Treatment with ABR, ABR-NP, and Apt-ABR-NP significantly reduced PSMA content in blood (15.1 ± 1.2, 12.3 ± 0.9, 7 ± 0.5 ng/ml, respectively). CRP data showed higher level of it in cancer-bearing animals suggesting development of inflammatory conditions. Treating with the experimental nanoparticles resulted lowering of the CRP levels in the blood.

Estimation of serum-specific toxicity markers

The levels of serum AST, ALT, and ALP often reveal whether the liver is healthy or diseased (Dhara et al. 2023). In this case, compared to the normal mice, mice exposed to carcinogen had higher serum levels of AST, ALT, and ALT. Carcinogen-treated mice, after the treatment with ABR, ABR-NP, and Apt-ABR-NP, the levels of the enzymes, creatinine and BUN were variably reduced. Additional file 1: Table-S5 reveals that Gr E animals (carcinogenic animals treated with Apt-ABR-NP) had improved to the greatest extent. Additionally, there were no appreciable modifications in Apt-ABR-NP-treated normal mice (Gr F animals) with normal serum AST, ALT, and ALP values. When creatinine and BUN levels in blood serum were measured, the results observed were similar.

The data suggest that the treatment of ABR, ABR-NP and Apt-ABR-NP improved the hepatic and nephrotic toxicity of mice treated with carcinogen. Among the ABR treatment groups Apt-ABR-NP-treated mice showed maximum improvement of the enzyme levels and creatinine and BUN towards the normal values. Normal mice did not show any significant differences in the enzyme levels and concentrations of the creatinine and BUN compared to the normal mice received Apt-ABR-NP treatment. Thus, it suggests Apt-ABR-NP did not show any toxicity in liver and kidneys of normal animals.

The existing therapies, including hormone therapy, surgery, radiation therapy, chemotherapy, etc., have some disadvantages. One such disadvantage is the lack of targeted treatment, i.e., off-target toxicity. Aptamers are called synthetic monoclonal antibodies for their target specificity, but without the toxicity problem. In our research, we have targeted prostate-specific membrane antigen (PSMA) that overexpresses in prostate cancer cells. The anti-PSMA aptamer conjugated formulation specifically binds to the overexpressed PSMA in the cancer cells for the target specific delivery of the drug. So, our designed nanoparticles could be a promising approach for treating prostate cancer and have an edge over the existing formulations.

Conclusion

A recently discovered aptamer (ΔPSap4#5) was conjugated with ABR-NP (Apt-ABR-NP) that predominantly accumulated to PSMA overexpressed prostate cancer. This is the first study in which this aptamer was considered for prostate cancer treatment. Apt-ABR-NP showed better cellular internalization than the non-conjugated formulation. Apt-ABR-NP ensured successful site-specific drug delivery to PSMA-overexpressed prostate cancer cells, Apt-ABR-NP exhibited prolonged blood retention, sustained drug release, and tumor tissue-specific accumulation. The findings presented the aptamer-coupled nanoparticulated therapeutic technique that demonstrated the maximum in vitro and in vivo therapeutic effectiveness of Apt-ABR-NP. We anticipate for a hope of translation of the promising aptamer functionalized nanoparticle toward achieving successful human clinical trials in near future as a possible targeted treatment for prostate cancer. Further studies are warranted.

Abbreviations

Apt-ABR-NP	Aptamer conjugated abiraterone acetate nanoparticles
ABR	Abiraterone acetate
PLGA	Poly(D,L-lactide-*co*-glycolide)
PCa	Prostate cancer
FTIR	Fourier transform infrared spectroscopy
FESEM	Field emission scanning electron microscopy
HR-TEM	High-resolution transmission electron microscopy
AFM	Atomic force microscopy
XPS	X-ray photoelectron spectroscopy
FITC	Fluorescein isothiocyanate
PI	Propidium iodide
AUC	Area under the curve

Supplementary Information

The online version contains supplementary material available at https://doi.org/10.1186/s12645-023-00223-5.

> **Additional file 1.** Detailed methodology (Preparation of the PLGA nanoparticles, Conjugation of aptamer on the surface of nanoparticles, Determination of aptamer conjugation by agarose gel electrophoresis, Percentage of drug loading and encapsulation efficiency, Stability of the nanoparticles, Hydrolytic stability study, In vitro drug release study), Table S1, Table S2, Table S3, Table S4 and Table S5; Figure S1, Figure S2 and Figure S3.

Author contributions

AAH and BM developed the concept and design of the project. Synthesis and physicochemical characterizations were performed by AAH, DD, LK, and IE. Agarose gel electrophoresis was performed by AAH and MD. AAH, DD, and BP performed cell assays with the guidance of MQ and BK. SL was associated with LC–MS analysis. In vivo experiments were performed by AAH, BP, and SG. Analysis and interpretation of the data included the contribution of all authors. The manuscript was written by AAH and DD, and edited and revised by BM and MQ. All authors have approved the final version of the manuscript.

Availability of data and materials

All data in this study are available from the corresponding authors upon reasonable request.

Declarations

Ethics approval and consent to participate

Permission from the Institutional Animal Ethics Committee (IAEC) of Jadavpur University was received before commencing any animal experiments ((JU-IAEC, Protocol approval. no.: AEC/PHARM/1704/04/2020), under the norms of CPCSEA, Govt. of India (Jadavpur University Registration Number in CPCSEA: 1805/G.O./Re/S/15/CPCSEA). All experiments have been conducted following the guidelines of the Animal Ethics Committee of Jadavpur University.

Consent for publication
Not applicable.

Competing interests
The authors declare no conflict of interest.

References

Adamiecki R, Hryniewicz-Jankowska A, Ortiz MA, Li X, Porter-Hansen BA, Nsouli I et al (2022) In vivo models for prostate cancer research. Cancers (basel) 14(21):1–27

Alshaer W, Hillaireau H, Fattal E (2018) Aptamer-guided nanomedicines for anticancer drug delivery. Adv Drug Deliv Rev 134:122–137

Benoist GE, Hendriks RJ, Mulders PFA, Gerritsen WR, Somford DM, Schalken JA et al (2016) Pharmacokinetic aspects of the two novel oral drugs used for metastatic castration-resistant prostate cancer: abiraterone acetate and enzalutamide. Clin Pharmacokinet 55(11):1369–1380

Berlin A, Castro-Mesta JF, Rodriguez-Romo L, Hernandez-Barajas D, González-Guerrero JF, Rodríguez-Fernández IA et al (2017) Prognostic role of Ki-67 score in localized prostate cancer: a systematic review and meta-analysis. Urol Oncol Semin Orig Investig 35(8):499–506

BIOVIA Discovery Studio—BIOVIA—Dassault Systèmes®

Bouhajib M, Tayab Z (2019) Evaluation of the pharmacokinetics of abiraterone acetate and abiraterone following single-dose administration of abiraterone acetate to healthy subjects. Clin Drug Investig 39(3):309–317

Chakraborty S, Dlie ZY, Chakraborty S, Roy S, Mukherjee B, Besra SE et al (2020a) Aptamer-functionalized drug nanocarrier improves hepatocellular carcinoma toward normal by targeting neoplastic hepatocytes. Mol Ther Nucleic Acids 20:34–49

Chakraborty S, Dlie ZY, Mukherjee B, Besra SE, Sengupta S, Sen R et al (2020b) A comparative investigation of the ability of various aptamer-functionalized drug nanocarriers to induce selective apoptosis in neoplastic hepatocytes: in vitro and in vivo outcome. AAPS PharmSciTech 21(3):1–13

Champion JA, Katare YK, Mitragotri S (2007) Particle shape: a new design parameter for micro- and nanoscale drug delivery carriers. J Control Release 121(1–2):3–9

Chen ML, Lai CJ, Lin YN, Huang CM, Lin YH (2020) Multifunctional nanoparticles for targeting the tumor microenvironment to improve synergistic drug combinations and cancer treatment effects. J Mater Chem B 8(45):10416–10427

Choi WI, Lee JH, Kim JY, Heo SU, Jeong YY, Kim YH et al (2015) Targeted antitumor efficacy and imaging via multifunctional nano-carrier conjugated with anti-HER2 trastuzumab. Nanomed Nanotechnol Biol Med 11(2):359–368

Clogston JD, Patri AK (2011) Zeta potential measurement. Methods Mol Biol 697:63–70

Correa S, Dreaden EC, Gu L, Hammond PT (2016) Engineering nanolayered particles for modular drug delivery. J Control Release 240:364–386

Danhier F, Ansorena E, Silva JM, Coco R, Le Breton A, Préat V (2012) PLGA-based nanoparticles: an overview of biomedical applications. J Control Release 161(2):505–522

Dassie JP, Liu XY, Thomas GS, Whitaker RM, Thiel KW, Stockdale KR et al (2009) Systemic administration of optimized aptamer-siRNA chimeras promotes regression of PSMA-expressing tumors. Nat Biotechnol 27(9):839–846

Dhara M, Al Hoque A, Sen R, Dutta D, Mukherjee B, Paul B et al (2023) Phosphorothioated amino-AS1411 aptamer functionalized stealth nanoliposome accelerates bio-therapeutic threshold of apigenin in neoplastic rat liver: a mechanistic approach. J Nanobiotechnol 21(1):28

Diepstraten ST, Anderson MA, Czabotar PE, Lessene G, Strasser A, Kelly GL (2022) The manipulation of apoptosis for cancer therapy using BH3-mimetic drugs. Nat Rev Cancer 22(1):45–64

Dutta D, Chakraborty A, Mukherjee B, Gupta S (2018) Aptamer-conjugated apigenin nanoparticles to target colorectal carcinoma: a promising safe alternative of colorectal cancer chemotherapy. ACS Appl Bio Mater 1(5):1538–1556

Dutta D, Paul B, Mukherjee B, Mondal L, Sen S, Chowdhury C et al (2019) Nanoencapsulated betulinic acid analogue distinctively improves colorectal carcinoma in vitro and in vivo. Sci Rep 9(1):11506

Ehsan I, Kumari L, Sen R, Al Hoque A, Mukherjee B, Mukherjee A et al (2022) J591 functionalized paclitaxel-loaded PLGA nanoparticles successfully inhibited PSMA overexpressing LNCaP cells. J Drug Deliv Sci Technol 75:103689

Fan L, Campagnoli S, Wu H, Grandi A, Parri M, De Camilli E et al (2015) Negatively charged AuNP modified with monoclonal antibody against novel tumor antigen FAT1 for tumor targeting. J Exp Clin Cancer Res 34(1):103

Fan L, Gong Y, He Y, Gao WQ, Dong X, Dong B et al (2022) TRIM59 is suppressed by androgen receptor and acts to promote lineage plasticity and treatment-induced neuroendocrine differentiation in prostate cancer. Oncogene 42(8):559–571

Gala U, Miller D, Williams RO (2020) Improved dissolution and pharmacokinetics of abiraterone through kinetisol® enabled amorphous solid dispersions. Pharmaceutics 12(4):357

Gray BP, Kelly L, Ahrens DP, Barry AP, Kratschmer C, Levy M et al (2018) Tunable cytotoxic aptamer–drug conjugates for the treatment of prostate cancer. Proc Natl Acad Sci USA 115(18):4761–4766

Hashemi M, Shamshiri A, Saeedi M, Tayebi L, Yazdian-Robati R (2020) Aptamer-conjugated PLGA nanoparticles for delivery and imaging of cancer therapeutic drugs. Arch Biochem Biophys 691:108485

Hazra RS, Dutta D, Mamnoon B, Nair G, Knight A, Mallik S et al (2021) Polymeric composite matrix with high biobased content as pharmaceutically relevant molecular encapsulation and release platform. ACS Appl Mater Interfaces 13(34):40229–40248

Heydari-Bafrooei E, Shamszadeh NS (2017) Electrochemical bioassay development for ultrasensitive aptasensing of prostate specific antigen. Biosens Bioelectron 91:284–292

Huang D, Sun L, Huang L, Chen Y (2021) Nanodrug delivery systems modulate tumor vessels to increase the enhanced permeability and retention effect. J Pers Med 11(2):1–26

Jain GK, Pathan SA, Akhter S, Ahmad N, Jain N, Talegaonkar S et al (2010) Mechanistic study of hydrolytic erosion and drug release behaviour of PLGA nanoparticles: influence of chitosan. Polym Degrad Stab 12(95):2360–2366

Kabanov AV, Batrakova EV (2008) Polymer nanomaterials. In: Neuroimmune Pharmacology, pp 691–707

Kato M, Sasaki T, Inoue T (2021) Current experimental human tissue-derived models for prostate cancer research. Int J Urol 28(2):150–162

Krishnan V, Venkatasubbu GD, Kalaivani T, Krishnan V, Venkatasubbu GD, Kalaivani T (2023) Investigation of hemolysis and antibacterial analysis of curcumin-loaded mesoporous SiO2 nanoparticles. Appl Nanosci 13(1):811–818

Kumari L, Ehsan I, Mondal A, Al Hoque A, Mukherjee B, Choudhury P et al (2023) Cetuximab-conjugated PLGA nanoparticles as a prospective targeting therapeutics for non-small cell lung cancer. J Drug Target 31(5):521–536

Lawrence MG, Pook DW, Wang H, Porter LH, Frydenberg M, Kourambas J et al (2015) Establishment of primary patient-derived xenografts of palliative TURP specimens to study castrate-resistant prostate cancer. Prostate 75(13):1475–1483

Li YJ, Fahrmann JF, Aftabizadeh M, Zhao Q, Tripathi SC, Zhang C et al (2022) Fatty acid oxidation protects cancer cells from apoptosis by increasing mitochondrial membrane lipids. Cell Rep 39(9):110870

Liu J, Kopečková P, Bühler P, Wolf P, Pan H, Bauer H et al (2009) Biorecognition and subcellular trafficking of HPMA copolymer-anti-PSMA antibody conjugates by prostate cancer cells. Mol Pharm 6(3):959–970

Luo D, Wang X, Zeng S, Ramamurthy G, Burda C, Basilion JP (2019a) Prostate-specific membrane antigen targeted gold nanoparticles for prostate cancer radiotherapy: does size matter for targeted particles? Chem Sci 10(35):8119–8128

Luo X, Yang Y, Kong F, Zhang L, Wei K (2019b) CD30 aptamer-functionalized PEG-PLGA nanoparticles for the superior delivery of doxorubicin to anaplastic large cell lymphoma cells. Int J Pharm 564:340–349

Madani SH, Ameli S, Khazaei S, Kanani M, Izadi B (2011) Frequency of Ki-67 (MIB-1) and P53 expressions among patients with prostate cancer. Indian J Pathol Microbiol 54(4):688–691

Mukherjee B, Mayer D (2008) Dihydrotestosterone interacts with EGFR/MAPK signalling and modulates EGFR levels in androgen receptor-positive LNCaP prostate cancer cells. Int J Oncol 33(3):623–629

Munjal A, Leslie SW (2023) Gleason score. Encycl Genet genomics, proteomics informatics. StatPearls Publishing, pp 800–800

Nahata A, Dixit VK (2012) Ganoderma lucidum is an inhibitor of testosterone-induced prostatic hyperplasia in rats. Andrologia 44:160–174

Pagels RF, Prud'Homme RK (2015) Polymeric nanoparticles and microparticles for the delivery of peptides, biologics, and soluble therapeutics. J Control Release 219:519–535

Panyam J, Zhou W, Prabha S, Sahoo SK, Labhasetwar V (2002) Rapid endo-lysosomal escape of poly(DL-lactide-co glycolide) nanoparticles: implications for drug and gene delivery. FASEB J 16(10):1217–1226

Papachristou F, Anninou N, Koukoulis G, Paraskakis S, Sertaridou E, Tsalikidis C et al (2021) Differential effects of cisplatin combined with the flavonoid apigenin on HepG2, Hep3B, and Huh7 liver cancer cell lines. Mutat Res Genet Toxicol Environ Mutagen 866:503352

Pattnaik G, Sinha B, Mukherjee B, Ghosh S, Basak S, Mondal S et al (2012) Submicron-size biodegradable polymer-based didanosine particles for treating HIV at early stage: an in vitro study. J Microencapsul 29(7):666–676

Paul B, Gaonkar RH, Mukhopadhyay R, Ganguly S, Debnath MC, Mukherjee B (2019) Garcinol-loaded novel cationic nanoliposomes: in vitro and in vivo study against B16F10 melanoma tumor model. Nanomedicine (lond) 14(15):2045–2065

Petros RA, Desimone JM (2010) Strategies in the design of nanoparticles for therapeutic applications. Nat Rev Drug Discov 9(8):615–627

Pierorazio PM, Walsh PC, Partin AW, Epstein JI (2013) Prognostic Gleason grade grouping: data based on the modified Gleason scoring system. BJU Int 111(5):753–760

Pokrovsky VS, Zolottsev VA, Latysheva AS, Kudinov VA, Anisimova NY, Almanza RLM et al (2020) Alsevirone-NF reduces serum testosterone and inhibits prostate cancer xenograft growth in Balb/c nude mice. Clin Cancer Drugs 7(2):113–118

Ramdhani D, Listiani N, Sriyani ME, Maria WE, Watabe H, Mustarichie R et al (2023) Estrogen receptor targeting with genistein radiolabeled Technetium-99m as radiotracer of breast cancer: Its optimization, characterization, and predicting stability constants by DFT calculation. Heliyon 9(2):e13169

Rockey WM, Hernandez FJ, Huang SY, Cao S, Howell CA, Thomas GS et al (2011) Rational truncation of an RNA aptamer to prostate-specific membrane antigen using computational structural modeling. Nucleic Acid Ther 21(5):299–314

Ruoslahti E, Bhatia SN, Sailor MJ (2010) Targeting of drugs and nanoparticles to tumors. J Cell Biol 188(6):759–768

Savory N, Abe K, Sode K, Ikebukuro K (2010) Selection of DNA aptamer against prostate specific antigen using a genetic algorithm and application to sensing. Biosens Bioelectron 26(4):1386–1391

Schleicher RL, Fallon MT, Austin GE, Zheng M, Zhang M, Dillehay DL et al (1996) Intravenous vs Intraprostatic administration of N-methyl-N-nitrosourea to induce prostate cancer in rats MNU-induced prostate cancer in rats. Aff Med Cent 28:32–75

Sen R, Mukherjee B, Ganguly S, Sinha S (2023) Surface-functionalized luteolin-loaded nanocarriers successfully delayed lung cancer progress in rats. J Mater Sci 58(18):7731–7757

Shah B, Khunt D, Misra M (2021) Comparative evaluation of intranasally delivered quetiapine loaded mucoadhesive microemulsion and polymeric nanoparticles for brain targeting: pharmacokinetic and gamma scintigraphy studies. Futur J Pharm Sci 7(1):1–12

Shahriari M, Taghdisi SM, Abnous K, Ramezani M, Alibolandi M (2021) Self-targeted polymersomal co-formulation of doxorubicin, camptothecin and FOXM1 aptamer for efficient treatment of non-small cell lung cancer. J Control Release 335:369–388

Shishparenok AN, Furman VV, Zhdanov DD (2023) DNA-based nanomaterials as drug delivery platforms for increasing the effect of drugs in tumors. Cancers (basel) 15(7):1–58

Solymosi T, Tóth F, Orosz J, Basa-Dénes O, Angi R, Jordán T et al (2018) Solubility measurements at 296 and 310 K and physicochemical characterization of abiraterone and abiraterone acetate. J Chem Eng Data 63(12):4453–4458

Souada M, Piro B, Reisberg S, Anquetin G, Noël V, Pham MC (2015) Label-free electrochemical detection of prostate-specific antigen based on nucleic acid aptamer. Biosens Bioelectron 68:49–54

Sung H, Ferlay J, Siegel RL, Laversanne M, Soerjomataram I, Jemal A et al (2021) Global Cancer Statistics 2020: GLOBOCAN estimates of incidence and mortality worldwide for 36 cancers in 185 countries. CA Cancer J Clin 71(3):209–249

Tătaru OS, Martha O, Crocetto F, Barone B, Voidazan S, Borda A et al (2021) Fascin-1 and its role as a serological marker in prostate cancer: a prospective case–control study. Future Sci OA 7(9):FSO745

Thasneem YM, Sajeesh S, Sharma CP (2011) Effect of thiol functionalization on the hemo-compatibility of PLGA nanoparticles. J Biomed Mater Res A 99(4):607–617

Tong R, Gabrielson NP, Fan TM, Cheng J (2012) Polymeric nanomedicines based on poly(lactide) and poly(lactide-co-glycolide). Curr Opin Solid State Mater Sci 16(6):323–332

Torchilin VP (2007) Targeted pharmaceutical nanocarriers for cancer therapy and imaging. AAPS J 9:E128–E147

Tuerk C, Gold L (1990) Systematic evolution of ligands by exponential enrichment: RNA ligands to bacteriophage T4 DNA polymerase. Science 249(4968):505–510

Tzouvadaki I, Jolly P, Lu X, Ingebrandt S, De Micheli G, Estrela P et al (2016) Label-free ultrasensitive memristive aptasensor. Nano Lett 16(7):4472–4476

Volpatti LR, Yetisen AK (2014) Commercialization of microfluidic devices. Trends Biotechnol 32(7):347–350

Wan LY, Yuan WF, Ai WB, Ai YW, Wang JJ, Chu LY et al (2019) An exploration of aptamer internalization mechanisms and their applications in drug delivery. Expert Opin Drug Deliv 16(3):207–218

Wang Y, Li P, Kong L (2013) Chitosan-modified PLGA nanoparticles with versatile surface for improved drug delivery. AAPS PharmSciTech 14(2):585–592

Wang R, Chu GCY, Wang X, Wu JB, Hu P, Multani AS et al (2019) Establishment and characterization of a prostate cancer cell line from a prostatectomy specimen for the study of cellular interaction. Int J Cancer 145(8):2249–2259

Weatherby D, Ferguson S (2004) Blood chemistry and CBC analysis. Weatherby & Associates, Bloomfield

Wolff A, Frank M, Staehlke S, Peters K (2022) A comparative study on the adipogenic differentiation of mesenchymal stem/stromal cells in 2D and 3D culture. Cells 11(8):1313

Yadav KS, Sawant KK (2010) Modified nanoprecipitation method for preparation of cytarabine-loaded PLGA nanoparticles. AAPS PharmSciTech 11(3):1456

Yallapu MM, Khan S, Maher DM, Ebeling MC, Sundram V, Chauhan N et al (2014) Anti-cancer activity of curcumin loaded nanoparticles in prostate cancer. Biomaterials 35(30):8635–8648

Yan Y, Tao H, He J, Huang SY (2020) The HDOCK server for integrated protein–protein docking. Nat Protoc 15(5):1829–1852

Yang S, Cai C, Wang H, Ma X, Shao A, Sheng J et al (2022) Drug delivery strategy in hepatocellular carcinoma therapy. Cell Commun Signal 20(1):1–14

Yin J, Wang P, Yin Y, Hou Y, Song X (2017) Optimization on biodistribution and antitumor activity of tripterine using polymeric nanoparticles through RES saturation. Drug Deliv 24(1):1891–1897

Zununi Vahed S, Fathi N, Samiei M, Maleki Dizaj S, Sharifi S (2019) Targeted cancer drug delivery with aptamer-functionalized polymeric nanoparticles. J Drug Target 27(3):292–299

Publisher's Note